

Ray splitting and quantum chaos

Reinhold Blümel,^{1,*} T. M. Antonsen, Jr.,^{1,2} Bertrand Georgeot,^{1,†} Edward Ott,^{1,2,3} and R. E. Prange¹¹Department of Physics, University of Maryland, College Park, Maryland 20742²Department of Electrical Engineering and Institute for Plasma Research, University of Maryland, College Park, Maryland 20742³Institute for Systems Research, University of Maryland, College Park, Maryland 20742

(Received 21 September 1995)

Ray splitting is the phenomenon whereby a ray incident on a boundary splits into more than one ray traveling away from the boundary. The most common example of this is the situation, originally considered by Snell in 1621, in which an incident light ray splits into reflected and transmitted rays at a discontinuity in refractive index. This paper seeks to extend techniques and results from quantum chaos to short wavelength problems in which ray splitting surfaces are present. These extensions are tested using a simple model problem for the Schrödinger equation in two dimensions with a finite step potential discontinuity. Numerical solutions for the energy spectrum and eigenfunctions in this system are then compared with predictions based on quasiclassical theoretical results suitably extended to include ray splitting. Among the topics treated are the ray orbits for our problem, energy level statistics, scars, trace formulas, the quasiclassical transfer operator technique, and the effect of lateral waves. It is found that these extensions of quantum chaos are very effective for treating problems with ray splitting.

PACS number(s): 05.45.+b, 03.65.Sq

I. INTRODUCTION

The study of wave equations in the short-wavelength limit is important in many fields. Examples are seismology, acoustics, optics, microwaves, and, perhaps most notably, quantum mechanics. In the latter case the resulting approximate theories are referred to as *quasiclassical*. In general, short-wavelength problems are, to lowest order, addressed by ray equations that necessarily have a Hamiltonian form. Quasiclassical approximation techniques to the solutions of wave equations in the case of integrable ray Hamiltonians have been well developed for a long time. The study of the opposite case of chaotic ray Hamiltonians or ray Hamiltonians yielding a mixed chaotic-integrable phase space is much more recent [1–4]. This latter field of study, called quantum chaos, has been very active and notable successes have been achieved. The object of this paper is to consider and test extensions of previous successful quantum chaos techniques and results to a broad class of problems not previously extensively addressed by these techniques.

In particular, we study systems in which there exists a surface at which an incident ray is split into two or more rays propagating away from the surface [5,6]. For example, a light ray incident on a discontinuity of refractive index splits into a reflected ray and a transmitted ray [Fig. 1(a)]. This was first quantified by Snell in 1621. The same thing happens for a wave function solution of the Schrödinger equation incident on a discontinuity in potential. Elastic media support two types of waves, shear

(*S*) and pressure (*P*) waves, and when an elastic wave is incident on a clamped or free boundary, ray splitting occurs [Fig. 1(b) and Ref. [5]]. Elastic wave ray splitting as shown in Fig. 1(b) occurs in the interesting experimental papers in Refs. [7–9]. An example where a ray splits into four rays at a discontinuity between two elastic media is shown in Fig. 1(c). Another phenomenon typically associated with ray splitting boundaries is total internal reflection. In total internal reflection an incident wave is reflected, but acquires a phase shift. The totally internally reflected wave also results in an evanescent wave exponentially decreasing away from the boundary in the classically forbidden region. A third, much less well-known, phenomenon connected with ray splitting boundaries is the *lateral wave*. This will be briefly discussed in Sec. V.

To put the phenomena associated with ray splitting boundaries in perspective, we note that the standard justification of semiclassical approximations is based on the smallness of the parameter λ/a , where λ is the wave-

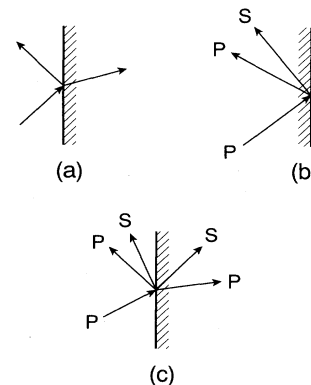


FIG. 1. Examples of ray splitting.

*Present address: Fakultät für Physik, Universität Albert-Ludwig, D79104 Freiburg, Germany.

†Present address: Neils Bohr Institute, Copenhagen ϕ , Denmark.

length and a is a representative classical length. However, there are often isolated places where this parameter is not small, for example, caustics and foci, and these cases can be satisfactorily dealt with. At a ray splitting boundary there is a change in medium properties that occurs over a distance $d \ll \lambda$. Thus ray splitting is fundamentally a wave (i.e., nonclassical) effect. We assume, however, that, aside from d , all other classical lengths (e.g., the curvature of the ray splitting surface) are large compared to the wavelength.

In this paper we concentrate on a particular model problem for the two-dimensional Schrödinger equation. We emphasize, however, that we believe the results to have general utility for other geometries and for wave equations other than the Schrödinger equation. The model situation we study is illustrated in Fig. 2. There is a circle of unit radius that is regarded as defining a circular potential well with infinitely high walls. In one half of the interior of the circle, $\pi/2 < \theta < 3\pi/2$, the potential vanishes. In the other half, $-\pi/2 < \theta < \pi/2$, the potential has a constant value $V_0 > 0$. In this "stepped" well we put a quantum particle of mass $m = \frac{1}{2}$. Setting $\hbar = 1$, the energy is $E = k_0^2$, where k_0 is the wave number in the zero potential region. We thus study the equation

$$[\nabla^2 + E - V_0 u(x)]\Psi = 0, \quad r \leq 1, \quad (1.1)$$

where $\Psi = 0$ at $r = 1$, $u(x)$ is the unit step function, and the rectangular coordinates (x, y) are as shown in Fig. 2. [For the case of a cylindrical electromagnetic cavity with the electric field parallel to the cylinder's axis and with dielectric of refractive index n_0 in $\pi/2 < \theta < 3\pi/2$, Eq. (1.1) applies if we replace E by the square of the wave number k_0^2 in the dielectric and V_0 by $k_0^2(1 - n_0^{-2})$.]

In Sec. II we discuss ray aspects of our model problem. We consider rays in two limits: (i) $\lambda \ll d$ (d still small compared to any other classical length) and (ii) $\lambda \gg d$. In case (i) the ray dynamics is classical and deterministic and there is no ray splitting. We find that, depending on the energy E , the phase space can be predominantly chaotic with only relatively small regions occupied by invariant tori. In case (ii) ray splitting is shown to destroy essentially all of the sizable tori, thus increasing ergodicity still further [5,6].

Following Sec. II, the rest of the paper considers solutions of the wave equation. For this purpose we utilized a simple numerical technique. The technique is to expand the wave function Ψ in an orthonormal basis for the circle with $\Psi = 0$ at $r = 1$ [sinusoidal functions of $m\theta$

multiplied by Bessel functions $J_m(k_{mp}r), J_m(k_{mp}) = 0$]. Truncation and projection onto the basis yields a finite matrix, which is then numerically diagonalized.

Section III considers spectral statistics for our numerically calculated energy levels. The Weyl result for our problem yields a spectral staircase function $N(E)$ that is linear in E for $E < V_0$ and $E > V_0$, but with a discontinuity in slope at $E = V_0$. Our numerical results agree well with this if a perimeter correction is included. We also verify good agreement of the nearest-neighbor level spacing distribution with the prediction of the Gaussian orthogonal ensemble [1-4]. Thus ray splitting apparently does not alter these well-established quantum chaos results. This has also been previously shown in the elastic wave experiments of Refs. [7-9] and in the numerical computations of Ref. [6].

In Sec. IV we present a pictorial display of large sequences of eigenfunctions (a "gallery of eigenfunctions"). We observe apparently ergodic eigenfunctions, along with many nonergodic (scarred [10]) eigenfunctions. Three types of scarred eigenfunctions emerge as particularly prominent.

- (i) Internal reflection scars in which the wave stays close to the ray splitting surface on the zero potential side.
- (ii) Whispering gallery scars in which the waves are guided by the outer wall at $r = 1$.
- (iii) Central bounce scars in which waves localized in angle apparently bounce radially between the wall and the center of the circle ($r = 0$).

The next two sections (Sec. V and VI) deal with quasiclassical approximation techniques.

The Gutzwiller trace formula is the standard quasiclassical approach to studies of the spectrum in quantum chaos. Recently it has been extended [5] to include ray splitting. This formula predicts that an appropriate scaled Fourier transform of the δ -function spectral density should exhibit sharp peaks at action values corresponding to periodic orbits. The difference here, as compared to previous work [11] exhibiting such action value peaks, is that ray splitting leads to different kinds of periodic orbits involving reflection, transmission, and total internal reflection. In Sec. V we find peaks of all three of these types in our numerical Fourier transform data. We also find evidence for a diffractivelike contribution called a *lateral ray* (e.g., see Appendix B and Ref. [12]).

The quasiclassical transfer operator technique [13,14] essentially provides a convenient way of counting and summing over classical paths. Section VI formulates and discusses the quasiclassical transfer operator for our problem in terms of direct, reflected, and transmitted ray contributions. Numerical implementation of the transfer operator for calculation of the spectrum yields good agreement with the full numerical calculations. This verifies the validity of the quasiclassical transfer operator technique for a ray splitting problem.

Section VII contains an analysis of the various types of scars discovered in Sec. V. It turns out that these scars can be quantitatively understood by use of the quasiclas-

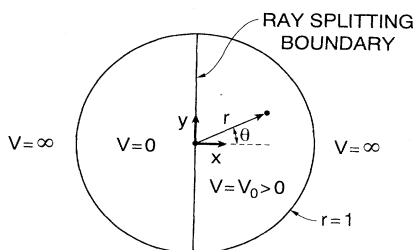


FIG. 2. Model problem.

sical transfer operator of Sec. VI.

In summary, the main message of this paper is that techniques and results developed for the study of problems in quantum chaos can be extended to apply to a wide class of practically important problems involving ray splitting boundaries. In addition, we find several phenomena associated with ray splitting, internal reflection (e.g., the internal reflection scars), and lateral rays [12].

II. RAYS

A. Deterministic rays

We first consider the ray problem for small wavelengths λ , but with $\lambda \ll d$, where d is the distance over which the potential in Fig. 2 increases from zero to $V_0 > 0$. That is, we consider the transition width from zero to V_0 to be classically negligible, but still large compared to a wavelength. In this limit there is no ray splitting and we have a classical orbit problem of the usual type. The effect of the boundary can be obtained from conservation of energy and of the momentum component parallel to the boundary. A particle of energy $E > V_0$ whose velocity vector makes angles of α_L and α_R to the normal to the boundary satisfies

$$\sqrt{E} \sin \alpha_L = \sqrt{E - V_0} \sin \alpha_R, \quad (2.1)$$

where α_L (α_R) applies to the left (right) of the boundary in Fig. 2. Equation (2.1) applies for $|\alpha_L|$ less than the angle for critical reflection α_c , where

$$\sin \alpha_c = \sqrt{1 - V_0/E}. \quad (2.2)$$

When $|\alpha_L| > \alpha_c$ a particle incident from the left is specularly reflected. If $E < V_0$ the particle is always on the left and is always specularly reflected from the boundary.

When $E < V_0$ the problem is that of a half-disk with no interior potential. This problem is completely integrable. When $E \gg V_0$ the dynamics is a slightly perturbed version of the integrable dynamics for the circle with $V_0 = 0$. Thus, for $E \gg V_0$, we expect (and numerically confirm) that most of the invariant tori for $V_0 = 0$ are preserved. Hence the interesting case is $E/V_0 > 1$, but not too large. Figure 3 shows a surface of section plot for $V_0 = 0.5E$. Here the surface of section is taken to be the outer boundary at $r = 1$ and the position on the boundary parameterized by θ is plotted horizontally and the angle $0 \leq \psi \leq \pi$ of the velocity vector to the counterclockwise tangent to the circle just after bouncing is plotted vertically (see Fig. 4).

The features evident in Fig. 3 are reflection symmetric about $\psi = \pi/2$ and about $\theta = \pi$. As can be seen from the figure, there is a large “chaotic sea” interspersed with island chains. The island chains contain invariant tori encircling elliptic periodic orbits. We see that the largest island chain is a period three chain located near $\psi = \psi_3$ in the figure (and, by reflection, there is also a period three chain near $\psi = -\psi_3$). Close inspection also yields less prominent island chains of period n near ψ values labeled ψ_n in the figure. Apparently ψ_n accumulates on $\psi = \pi$ as

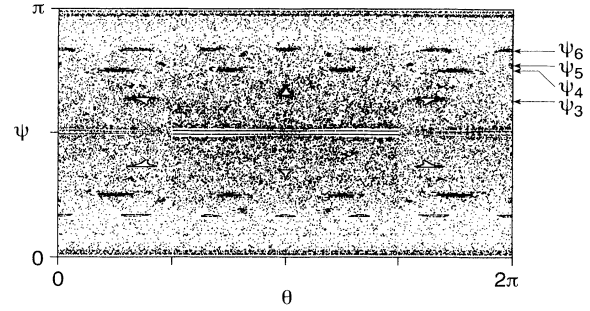


FIG. 3. Surface of section for deterministic ray orbits with $V_0 = 0.5E$. Fifty orbits are plotted with 10^3 iterates each.

n increases. The elliptic periodic orbits corresponding to islands of order $n = 3-6$ are shown in Fig. 5.

Two other features are also evident in Fig. 3. In particular, near $\psi = \pi/2$ we note an apparently horizontally striated structure. This structure is due to the presence of the neutrally stable continuous set of orbit families shown in Figs. 6(a) and 6(b), where in Fig. 6(a) the angles of incidence satisfy Eq. (2.1) and Fig. 6(b) corresponds to incidence at greater than the angle for critical reflection. The other important feature is the horizontally striated structure evident near $\psi = 0$ and π . This is associated with long epochs of time in which the chaotic orbit closely follows the circle at $r = 1$ (so-called “whispering gallery” motion). Because the orbit, although chaotic, experiences low exponential divergence while in whispering gallery motion, it takes a long time to leave this type of motion and a correspondingly long time to enter it. (This comment also applies to the orbits of Fig. 6.) Thus our numerical chaotic orbits of *finite duration* cover these regions nonuniformly. As we shall see subsequently (Sec. VII), both the orbits illustrated in Fig. 6, as well as those of the whispering gallery type, will result in significant wave function scars when we consider solutions of Eq. (1.1).

The features discussed above either prevent ergodicity (in the case of island chains) or lead to a slower rate of approach to it (in the case of the orbits of Fig. 6 and the whispering gallery motions). Nevertheless, most of the area of the surface of section in Fig. 3 appears to be fairly uniformly filled by the chaotic sea. Thus an orbit in the chaotic sea should be *approximately* ergodic over the energy surface. To test this, we first note that for a two-dimensional potential problem with potential $V(\mathbf{r})$ the assumption of ergodicity over the energy surface implies that the particle distribution function has uniform probability density per unit area in the allowed area $E \geq V(\mathbf{r})$ of configuration space and equal probability density in

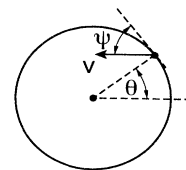


FIG. 4. Definition of ψ .

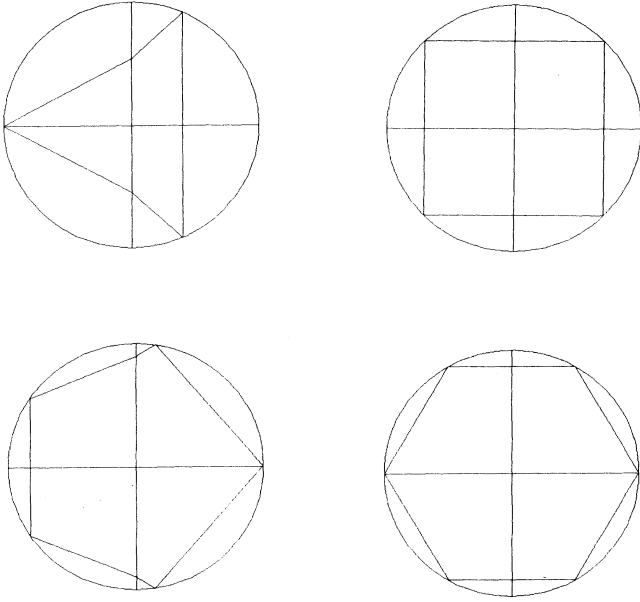


FIG. 5. Elliptic periodic orbits corresponding to island chains visible in Fig. 3.

the angular specification of the orientation of the momentum vector (e.g., Ref. [3], p. 352). Thus, for our problem (Fig. 2), if $E > V_0$, the particle probability density is uniform in $r \leq 1$. Note, however, that particles in the $V = V_0$ region move slower than particles in the $V = 0$ region. Thus there will be more orbit points in the surface of section corresponding to the $V = 0$ region (i.e., $\pi/2 < \theta < 3\pi/2$) than to the $V = V_0$ region. To obtain the expected fractions ρ_L and ρ_R of surface of section iterates on the left ($\pi/2 < \theta < 3\pi/2$) and right ($-\pi/2 < \theta < \pi/2$), we note that ρ_L and ρ_R are proportional to the probabili-

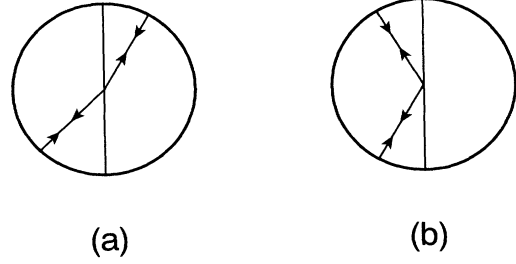


FIG. 6. Continuous sets of nonisolated orbits due to radial incidence on the boundary at the center of the circle.

ty flux into the boundary $r = 1$ in the left and right regions. Thus ρ_L/ρ_R is simply the ratio of the particle speeds in the left and right regions $\rho_L/\rho_R = \sqrt{E} / \sqrt{E - V_0}$. Using $\rho_L + \rho_R = 1$ we obtain

$$\rho_L = [1 + \sqrt{1 - \eta}]^{-1}, \tag{2.3}$$

where

$$\eta = V_0/E = \cos^2 \alpha_c.$$

Figure 7 shows Eq. (2.3) plotted as a solid curve with superposed plotted dots representing numerically determined ρ_L values obtained by following long orbits. Clearly the agreement is very good.

B. Ray dynamics with ray splitting

Because we solve Eq. (1.1) with an absolutely sharp boundary, the condition $\lambda \ll d$ used in Sec. II A, although instructive, does not apply. Rather we must take account of ray splitting. To do this we consider an infinite plane wave incident on an interface $x = 0$, where $V = 0$ in $x < 0$ and $V = V_0$ in $x > 0$,

$$\Psi = \begin{cases} [\exp(ik_L x \cos \alpha_L) + r_L(\alpha_L) \exp(-ik_L x \cos \alpha_L)] \exp(iky \sin \alpha_L) & \text{in } x < 0 \\ t_{LR}(\alpha) \exp[i(k_R x \cos \alpha_R) + i(k_R y \sin \alpha_R)] & \text{in } x > 0, \end{cases} \tag{2.4a}$$

$$\Psi = \begin{cases} t_{RL}(\alpha_R) \exp[-i(k_L x \cos \alpha_L) - i(k_L y \sin \alpha_L)] & \text{in } x < 0 \\ [\exp(-ik_R x \cos \alpha_R) + r_R(\alpha_R) \exp(ik_R x \cos \alpha_R)] \exp(-ik_R y \sin \alpha) & \text{in } x > 0. \end{cases} \tag{2.4b}$$

Here (2.4a) applies to a wave incident from the left ($x < 0$) while (2.4b) applies to a wave incident from the right; the wave numbers on the left and right are given by $k_L = \sqrt{E}$ and $k_R = \sqrt{E - V_0}$; the angles of incidence from the left α_L and right α_R are given by Snell's law, which is Eq. (2.1); (2.4a) applies for $|\alpha_L| \leq \alpha_c$. Continuity of Ψ and its normal derivative gives

$$r_L(\alpha_L) = -r_R(\alpha_R) = \frac{k_L \cos \alpha_L - k_R \cos \alpha_R}{k_L \cos \alpha_L + k_R \cos \alpha_R}, \tag{2.5}$$

and $t_{LR} = 1 + r_L$ and $t_{RL} = 1 + r_R$.

To study the ray dynamics, we imagine following a

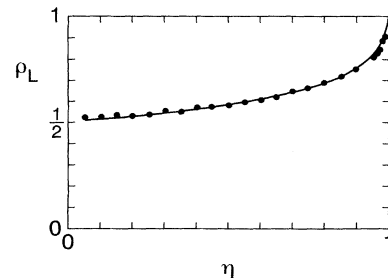


FIG. 7. ρ_L versus $\eta = V_0/E$ for the deterministic ray dynamics model ($\lambda \ll d$).

simple particle. When away from the ray splitting boundary the dynamics is classical; that is, the orbits are straight lines with specular reflection from the wall at $r=1$. When the particle ray is incident on the ray splitting boundary from the right-hand side, it is transmitted to the left-hand side with probability $1-r_R^2(\alpha_R)$ and reflected with probability $r_R^2(\alpha_R)$. When the particle ray is incident from the left at greater than the angle for critical reflection $|\alpha_L|>\alpha_c$, it is reflected; when $|\alpha_L|<\alpha_c$, it is transmitted with probability $1-r_L^2(\alpha_L)$ and reflected with probability $r_L^2(\alpha_L)$.

Thus we follow a ray and at each reflection use a random number generator to randomly decide with the appropriate probability whether to reflect or transmit the ray. Figure 8 shows a surface of section plot analogous to Fig. 3 using this stochastic ray dynamical procedure (see also Refs. [5,6]). We see that ray splitting apparently destroys the odd order invariant tori of Fig. 3, but leaves remnants of even order tori and also leaves the horizontally striated structures due to whispering gallery motion (near $\psi=0, \pi$), as well as those due to the radially bouncing rays (near $\psi=\pi/2$). Structures corresponding to the even order tori ($n=4, 6$) of Fig. 5 remain because ray splitting reflections send the orbit back along the same path (for n even, rays are normally incident on the boundary). In the case of ray splitting, the radially bouncing rays of Fig. 6(a) are replaced by the picture shown in Fig. 9.

Figure 10 shows a comparison of the ergodicity prediction for ρ_L (solid curve) with superposed dots calculated from long orbits using the ray splitting dynamics. As in Fig. 7, the agreement is very good, indicating that the ray spends equal amounts of time in the left region and in the right region. While this conclusion follows from the dynamics without ray splitting (in which case ergodicity implies a uniform distribution over the energy surface), it may not be clear that the same result applies for the case with ray splitting. To show that this is reasonable suppose that the distribution function is uniform in angle and uniform in the left (right) region with probability density per unit area f_L (f_R). We now show that $f_L=f_R$. The probability flux across the ray splitting boundary from left to right must equal that from right to left

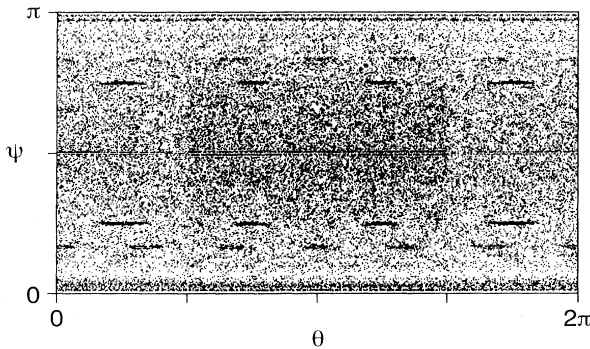


FIG. 8. Surface of section plot (analogous to Fig. 3) for stochastic ray orbits with $V_0=0.5E$.

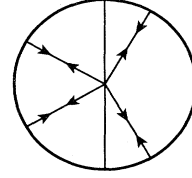


FIG. 9. Radially bouncing rays with reflection and transmission. The ray orbit, although stochastic (because of reflection and transmission probabilities), remains restricted to the four radial lines indicated for all time.

$$\int_{-\alpha_c}^{+\alpha_c} f_L \sqrt{E} \cos \alpha_L [1-r_L^2(\alpha_L)] \frac{d\alpha_L}{2\pi} = \int_{-\pi/2}^{+\pi/2} f_R \sqrt{E-V} \cos \alpha_R [1-r_R^2(\alpha_R)] \frac{d\alpha_R}{2\pi}.$$

Noting Snell's law and changing the variable of integration to $k_y = \sqrt{E} \sin \alpha_L = \sqrt{E-V} \sin \alpha_R$ on both sides we have

$$f_L \int_{-\sqrt{E-V}}^{+\sqrt{E-V}} [1-r_L^2(\alpha_L)] dk_y = f_R \int_{-\sqrt{E-V}}^{+\sqrt{E-V}} [1-r_R^2(\alpha_R)] dk_y.$$

From (2.5), $r_L^2=r_R^2$ and thus $f_L=f_R$.

III. SPECTRAL STATISTICS

We have solved Eq. (1.1) for the eigenfunctions Ψ_n and eigenvalues E_n . The lowest-order quasiclassical result for the smoothed level counting function giving the number of eigenvalues (energy levels) below a value E is [1-4]

$$\bar{N}(E) = V(E)/(2\pi\hbar)^D,$$

where D is the spatial dimensionality ($D=2$ for our case) and $V(E)$ is the volume of phase space within the energy surface

$$V(E) = \int \int u(E-H(\mathbf{p}, \mathbf{q})) d^2\mathbf{p} d^2\mathbf{q}.$$

Here $u(\cdot)$ denotes the unit step function and $H(\mathbf{p}, \mathbf{q})$ is the Hamiltonian. For our problem with $\hbar=1$ and $m=\frac{1}{2}$ we obtain

$$\bar{N}(E) = \frac{1}{8} [Eu(E) + (E-V_0)u(E-V_0)]. \quad (3.1a)$$

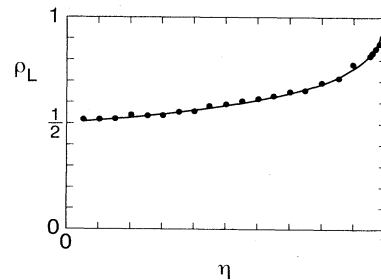


FIG. 10. ρ_L versus $\eta=V_0/E$ for ray splitting orbit (dots) compared with theory (solid curve).

Thus the average spacing between adjacent levels $[d\bar{N}(E)/dE]^{-1}$ is 8 for $E < V_0$ and 4 for $E > V_0$. Figure 11(a) compares (3.1) with our numerical data for the odd symmetry eigenvalues and $V_0 = 1000$ [restricting to either even or odd symmetry multiplies Eq. (3.1a) by $\frac{1}{2}$]. The result is much improved [Fig. 11(b)] if we incorporate the perimeter correction $\Delta\bar{N}(E)$ (see Ref. [1]). For a region of zero potential inside a billiard,

$$\Delta\bar{N}(E) = \mp (L/4\pi)(2mE/\hbar^2)^{1/2}, \quad (3.1b)$$

where L is the perimeter length and the minus (plus) sign

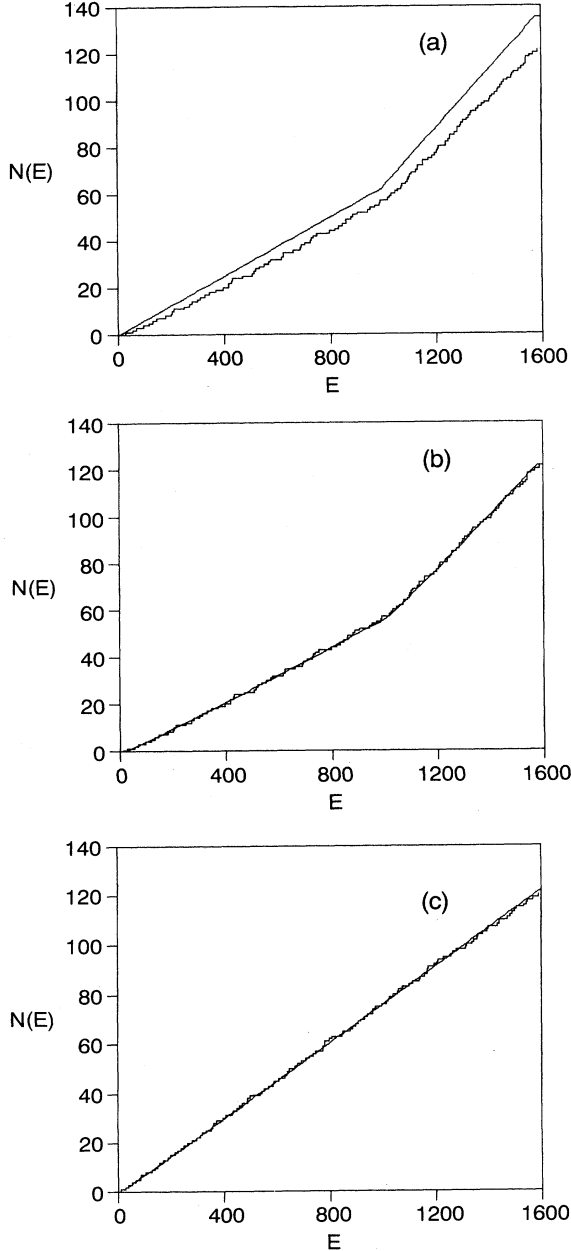


FIG. 11. $N(E)$ versus E for (a) the unscaled problem without the perimeter correction, (b) the unscaled problem with the perimeter correction, and (c) the scaled problem with the perimeter correction.

corresponds to Dirichlet (Neumann) boundary conditions on ψ . For the case of odd symmetry eigenfunctions we may regard the area as the upper half of the circle ($0 \leq \theta \leq \pi$) with $\psi = 0$ on the symmetry line ($\theta = 0, \pi$). The length of the effective boundary is $(\pi + 2)$ with one-half the length in the $V = 0$ region and one-half the length in the $V = V_0$ region. We thus obtain

$$\Delta\bar{N}(E) = -\frac{4}{\pi} \left[\frac{\pi}{2} + 1 \right] [\sqrt{E}u(E) + \sqrt{E - V_0}u \times (E - V_0)]. \quad (3.1c)$$

The result including the perimeter correction is shown in Fig. 11(b). The agreement is extremely good in spite of the fact that an additional correction (at the same order as the perimeter correction) occurs due to the ray splitting boundary [15]. Numerically, however, this correction is unobservably small for the case of Fig. 11 with our present statistics. In the case of even eigenfunctions the length factor $(\pi + 2)$ becomes $(\pi - 2)$, corresponding to a Neumann boundary condition on $\theta = 0, \pi$. In the even case similar good agreement with the numerical results is also obtained.

A standard prediction of quantum chaos is that the probability distribution function of the level spacings normalized to $[d\bar{N}(E)/dE]^{-1}$ is the same as that for the Gaussian orthogonal ensemble (GOE) of random matrices [1-4]. In our problem, however, we expect ray ergodicity to be very weak for $E \gg V_0$ because the step in potential is relatively unimportant in this case. Also for $E < V_0$ the ray dynamics in the half disk $\pi/2 < \theta < 3\pi/2$ is integrable. Thus to observe the GOE prediction we consider a restricted energy range for which the ray dynamics is observed to be approximately ergodic over the region within the circle. Figure 12 shows a histogram of the spacing distribution $P(S)$ for modes with odd parity about $\theta = 0, \pi$ with the GOE prediction plotted as a superposed smooth curve. This histogram is obtained using 3127 energy levels in the range $V_0 < E < V_0 + 200$ and 150 evenly spaced values of V_0 in the range $200 \leq V_0 \leq 299\frac{1}{3}$. Thus we confirm the GOE prediction for an example with ray splitting (see also Ref. [5]).

In order to avoid the variation of the character of the classical dynamics with energy E , we now considered a "scaled" problem. That is, we set $V_0/E = \eta$ and rewrite Eq. (1.1) as

$$[\nabla^2 + E(1 - \eta u(x))]\Psi = 0, \quad (3.2)$$

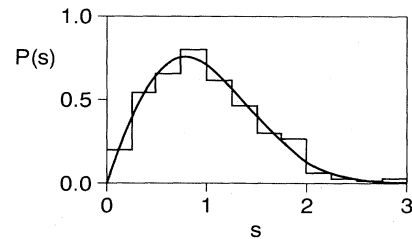


FIG. 12. $P(S)$ versus S using odd parity eigenfunctions for the unscaled problem.

where we now hold η fixed. The classical dynamics is invariant to changes of E and V_0 with $\eta = V_0/E$ fixed. [Note that this scaled problem for the Schrödinger equation corresponds precisely to the electromagnetic problem mentioned following Eq. (1.1).]

The numerical level counting function for the scaled problem is shown in Fig. 11(c) and closely follows the quasiclassical smoothed prediction, which results from setting $V_0 = \eta E$ in (3.1). For Fig. 11(c), $\eta = \frac{3}{4}$.

IV. GALLERY OF WAVE FUNCTIONS

Figure 13 shows a pictorial representation of odd parity wave functions Ψ_n for $n = 1-70$ with V_0 held fixed at

$V_0 = 200$. Values of n appear in the upper right of each wave function representation. The figure shows regions of high probability density $|\Psi_n|^2$ as darkened. We note that, as expected, for $E < V_0$, corresponding to the first few eigenfunctions ($n = 1-10$), most of the wave probability is located in the left half of the circle. Many of the eigenfunctions appear to be very irregular as one would expect from the ergodic nature of the ray dynamics for $n > 15$. In particular, we note the eigenfunctions of index $n = 23, 31, 39, 40, 41, 42$, and 57.

We also note the appearance of many eigenfunctions that deviate substantially from the prediction of ergodicity. In particular, we note the sequence shown in Fig. 14, where the n number is shown in the upper right of each

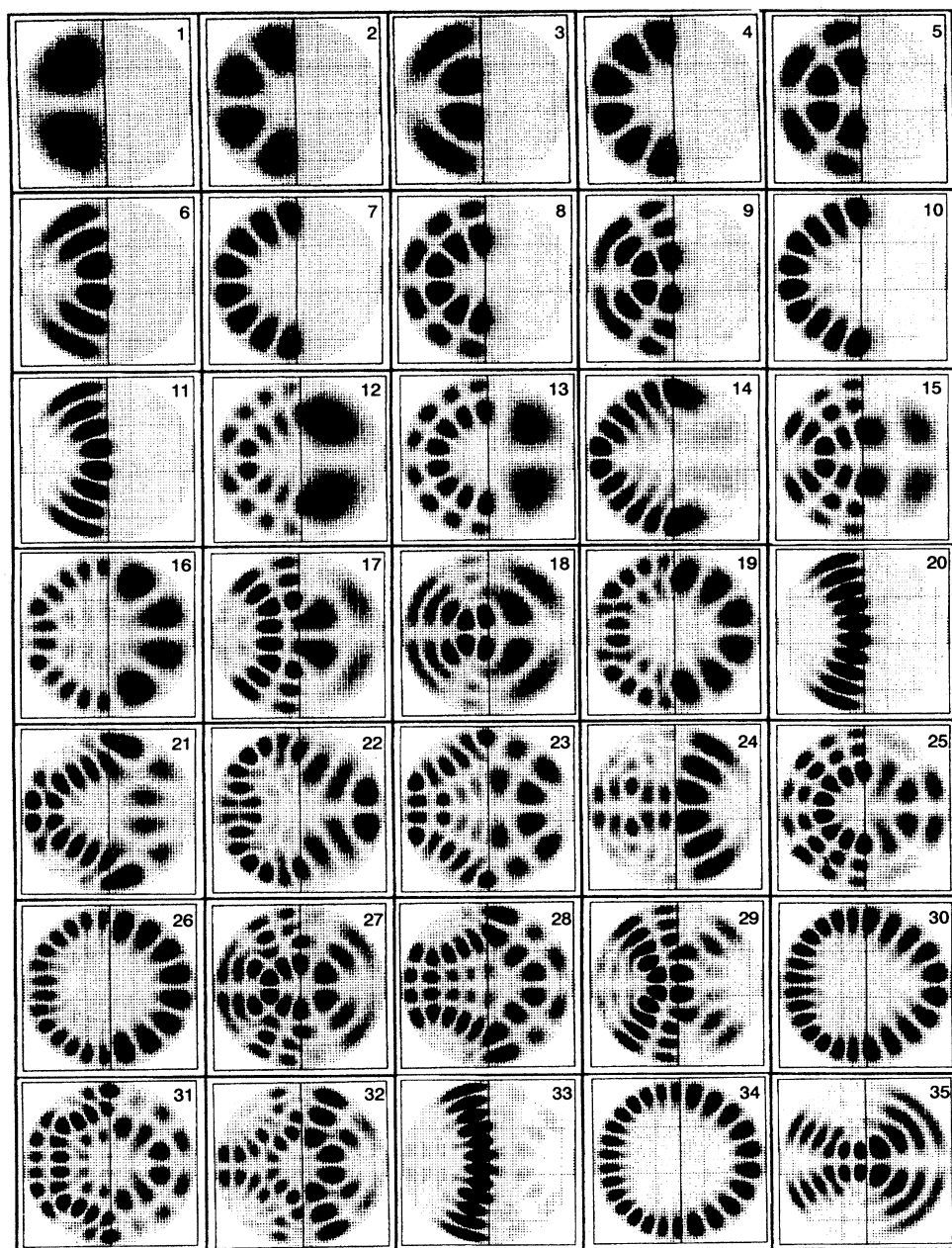


FIG. 13. Gallery of wave functions for $n = 1-70$ ($V_0 = 200$).

eigenfunction representation (n values of 1, 3, 6, 11, 20, 33, 49, and 67 already appear in Fig. 13) and an index p corresponding to this particular sequence is shown in the lower left. As we shall see (Sec. VII), these eigenfunctions may be associated with the internally reflecting ray shown in Fig. 6(b). We thus call these orbits internal reflection scars (IRS's). Whispering gallery scars (WIGS's) are also evident from Fig. 13, namely, $n = 2, 4, 7, 10, 14, 16, 26, 30, 34, 38, 43, 50, 54, 59,$ and 66 . With a little more imagination one can also identify a few scars that are apparently based on the centrally bouncing ray orbits of Fig. 9 ($n = 18, 24, 35,$ and 63). We call these central bounce scars (CBS's).

As discussed in Sec. VII, quantitative theories for the IRS's and WIGS's can be developed. For example, consider the energy levels E_p for the sequence of IRS wave functions in Fig. 14. We find numerically that these levels can be well fit by the equation

$$E_p = \pi^2 [p + \gamma_p]^2, \quad (4.1)$$

where, as shown in Fig. 15, the "defect" γ_p varies smoothly with p . The theory of Sec. VII will give an analysis yielding the solid approximation curve shown in the figure.

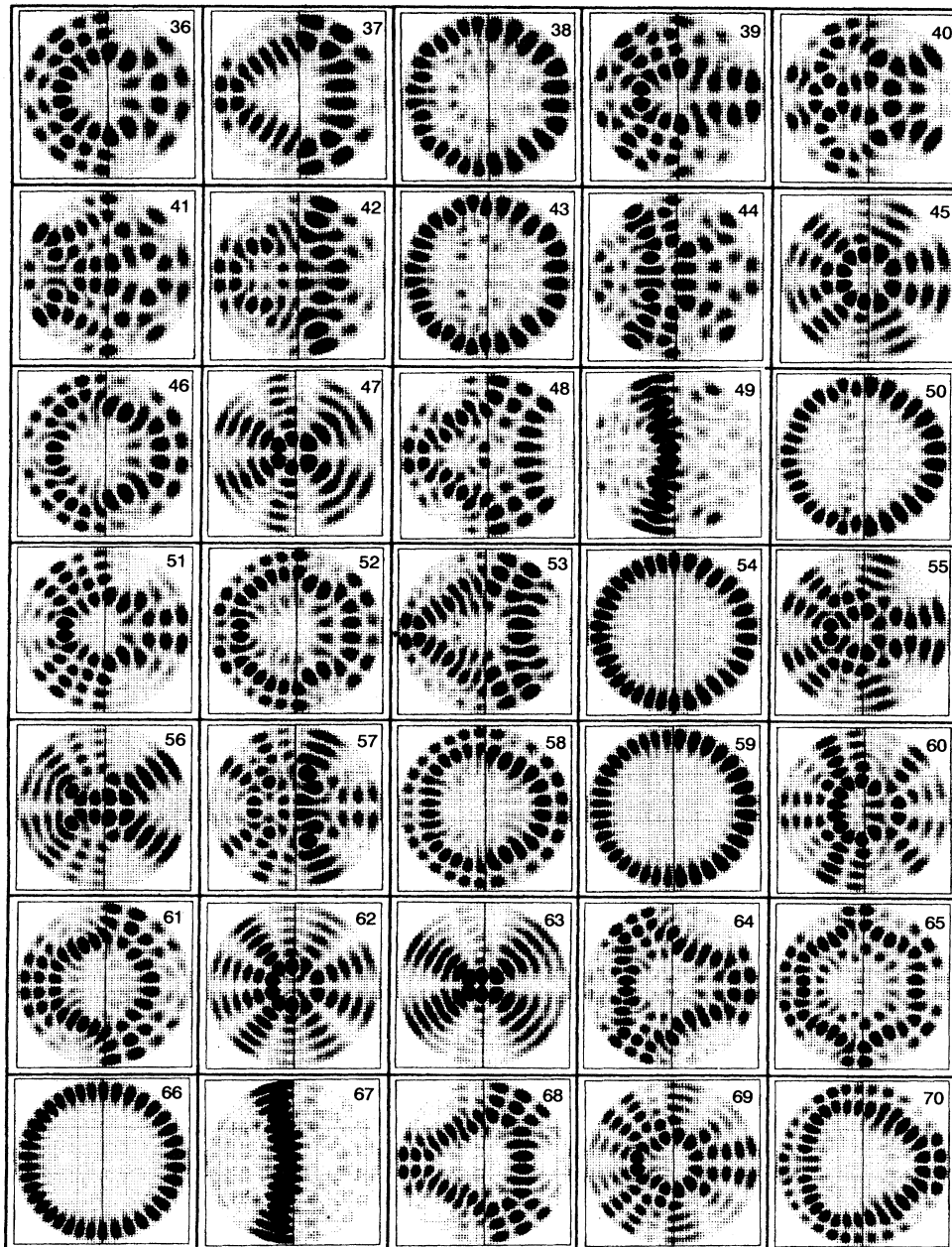


FIG. 13. (Continued).

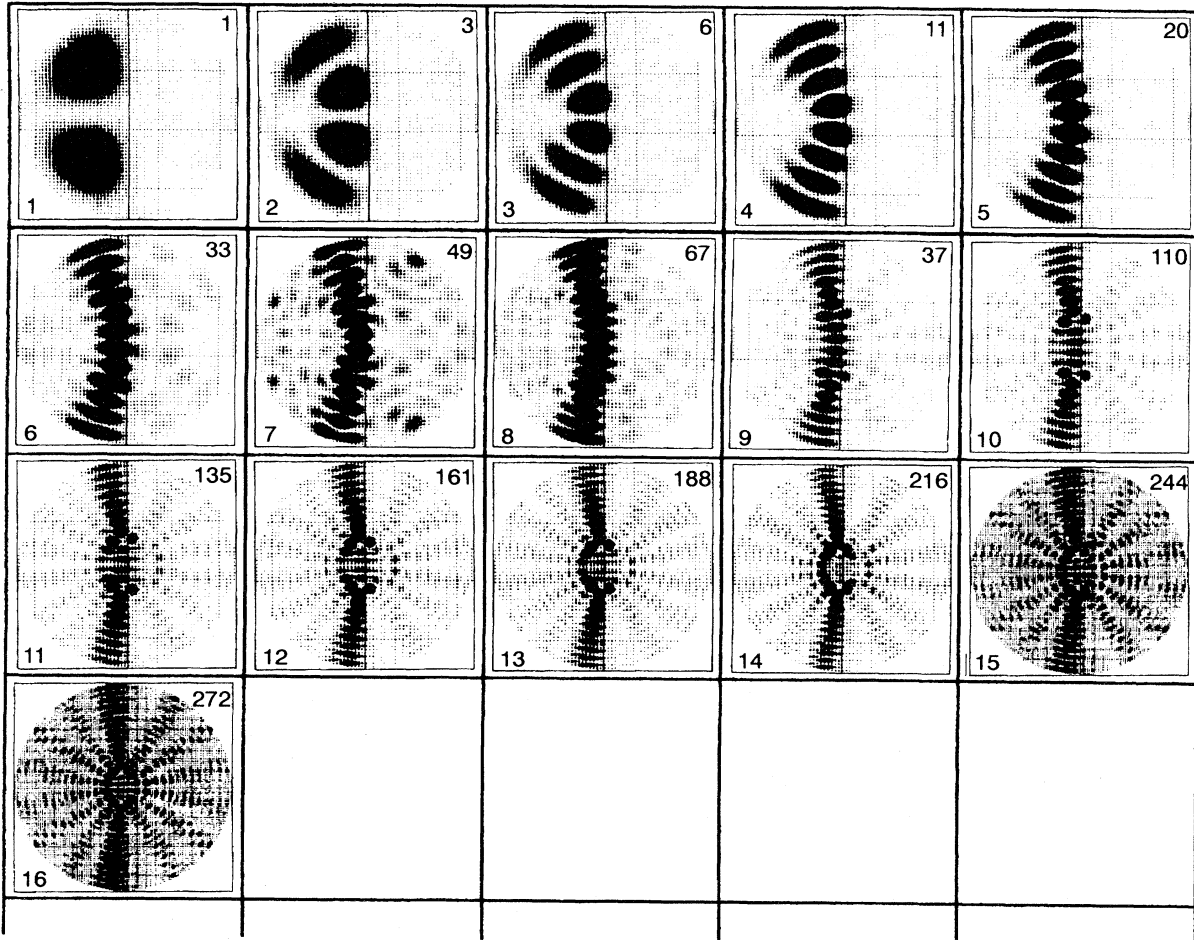
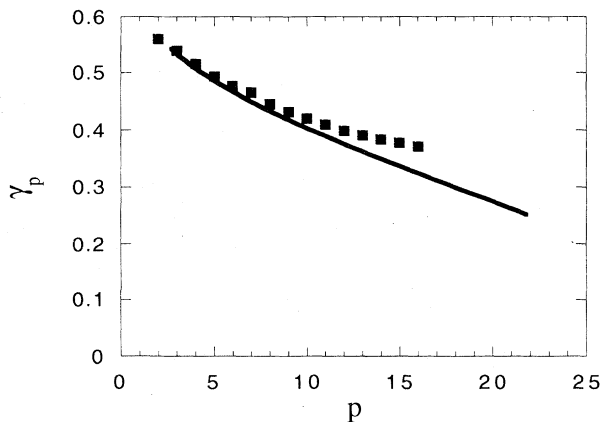
FIG. 14. Internal reflection scars ($V_0=200$).

FIG. 15. Defect γ_p defined in Eq. (4.1) versus quantum number p . The data points correspond to the numerically obtained eigenvalues and the solid line corresponds to the analytic solution for IRS's presented in Sec. VII.

V. THE QUASICLASSICAL APPROXIMATION: FOURIER TRANSFORM OF THE SPECTRUM

The Gutzwiller trace formula [1-4] for a problem without ray splitting has been extended to problems with ray splitting in Ref. [5]. The extended Gutzwiller formula (for isolated unstable periodic orbits) is

$$\bar{d}(E) \cong \text{Im} \left\{ \frac{1}{i\hbar} \sum_j \frac{(\hat{A}_j)^{1/2} T_j}{2 \sinh(\lambda_j/2)} \exp\{i[(S_j/\hbar) + \phi_j]\} \right\}, \quad (5.1)$$

where $\bar{d}(E)$ is an asymptotic approximation to the deviation of the density of states from the smoothed density $d\bar{N}(E)/dE$. The index j labels the discrete sets of closed periodic orbits. Here, by a periodic orbit we mean a closed ray path obtained for a periodic sequence of reflection-transmission decisions (some examples are shown in Fig. 16). The action is given by $S_j(E) = \oint \mathbf{p} \cdot d\mathbf{q}$,

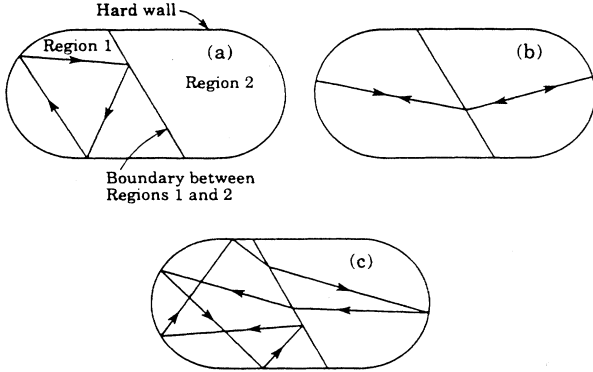


FIG. 16. Some closed orbits for a ray splitting stadium billiard corresponding to Schrödinger's equation with two homogeneous regions of different potential separated by the diagonal line shown.

where the integral is taken around periodic orbit j . T_j is the primitive period for periodic orbit j . $\lambda_j > 0$ is the stability exponent for orbit j ; it gives the exponential rate of increase of linearized perturbations of the orbit with the perturbed orbit satisfying conservation of tangential momentum at all transmissions (Snell's law) as well as angle of incidence equals angle of reflection at all reflections. The quantity \hat{A}_j is given by

$$\hat{A}_j = \left[\prod_{i=1}^{\hat{r}_j} |r_i|^2 \right] \left[\prod_{k=1}^{\hat{t}_j} (1 - |r_k|^2) \right], \quad (5.2)$$

where r_i is the reflection coefficient at the i th reflection of periodic orbit j , r_k is the reflection coefficient at the k th transmission of orbit j , and \hat{r}_j and \hat{t}_j are the number of reflections and transmissions for periodic orbit j . Thus \hat{A}_j is the quantum probability that a particle completes one circuit of the closed periodic orbit. For example, for the closed orbit in Fig. 16(a), $\hat{r}_j = 1$, $\hat{t}_j = 0$, and \hat{A}_j is $|r_a|^2$, where r_a is the reflection coefficient for the particular angle of incident for the ray in Fig. 16(a) incident on the boundary between the two regions; for the orbit in Fig. 16(b), $\hat{r}_j = 0$ and $\hat{t}_j = 2$; for the orbit in Fig. 16(c), $\hat{r}_j = 1$ and $\hat{t}_j = 2$. Finally, the phase ϕ_j includes the phases of all reflection coefficients, plus the usual Maslov contributions. In particular, if r_i is real and negative then the corresponding angle is π . Also, if there is critical reflection then r_i is complex with magnitude one, $r_i = \exp(i\Phi_i)$, and Φ_i adds a contribution to ϕ_j . (Note that there is no phase contribution on transmission because the transmission coefficient $1 - r_k$ is always positive for real r_k .)

Noting that $|\mathbf{p}| = \sqrt{E - V}$, the actions $S_j = \oint \mathbf{p} \cdot d\mathbf{q}$ can be expressed as

$$S_j = \sqrt{E} \sigma_j, \quad (5.3a)$$

where the scaled action σ_j is given by

$$\sigma_j = \mathcal{L}_{L_j} + \sqrt{1 - \eta} \mathcal{L}_{R_j}, \quad (5.3b)$$

with \mathcal{L}_{L_j} (\mathcal{L}_{R_j}) the path length of that part of the closed

orbit j that lies in the left (right) half of the circle. Considering the scaled problem [i.e., fixed η in Eq. (3.2)] the reduced actions are energy independent and the only energy dependence of the actions occurs in the overall multiplicative factor \sqrt{E} .

The transfer operator technique discussed in Sec. VI can be used to derive Eq. (5.1) and its generalizations to include nonisolated periodic orbits. This is discussed in Sec. VIA. The important point is that nonisolated periodic orbits make a contribution whose fast energy dependence is still $\exp[i(S_j/\hbar)]$ with S_j given by Eqs. (5.3).

Now consider the Fourier transform $F(\sigma)$ of the density of states with respect to \sqrt{E} ,

$$F(\sigma) = \int \tilde{d}(E) \exp(-i\sigma\sqrt{E}) d\sqrt{E}. \quad (5.4)$$

The extended Gutzwiller formula implies sharp peaks of $|F(\sigma)|^2$ occurring at the scaled actions [11] $\sigma = \sigma_j$.

Figure 17 shows a plot of $|F(\sigma)|^2$ obtained for $\eta = 0.5$ using energy levels of odd symmetry eigenfunctions in the range $0 \leq E \leq E_{\max}$, where E_{\max} corresponds to the 200th level. The computation utilized a windowing function $\sin[\pi\sqrt{E/E_{\max}}]$, inserted in the integrand of the Fourier transform for smoothing. Distinct peaks are clearly evident. The first eight of these peaks are labeled $\frac{1}{2}a$, $\frac{1}{2}b$, $\frac{1}{2}c$, d , b , e , f , and g . The numerical values of the actions at these peaks can be precisely identified with the corresponding orbits shown in Figs. 18(a)–18(g). The orbits in Figs. 18(a)–18(d) are nonisolated. The orbit shown as a solid line in Fig. 18(c1) arises as follows. If we imagine that the potential is zero everywhere in the circle, then the dashed square orbit in Fig. 18(c2) exists as part of a continuous family corresponding to rotation by an arbitrary angle. In the presence of the potential jump we can simply reflect that portion in $x > 0$ of the dashed orbit in Fig. 18(c2) through the potential jump boundary. The result [the solid curve in Fig. 18(c1)] automatically satisfies the condition (angle of incidence) = (angle of reflection) at the jump boundary. The same construction applies for any regular polygon [e.g., the reflected equilateral triangle in Fig. 18(h) is part of a nonisolated family]. Due to the up-down symmetry and our restriction to odd up-down parity modes for the data of Fig. 17, we can imagine that there is effectively a perfect reflector on the x

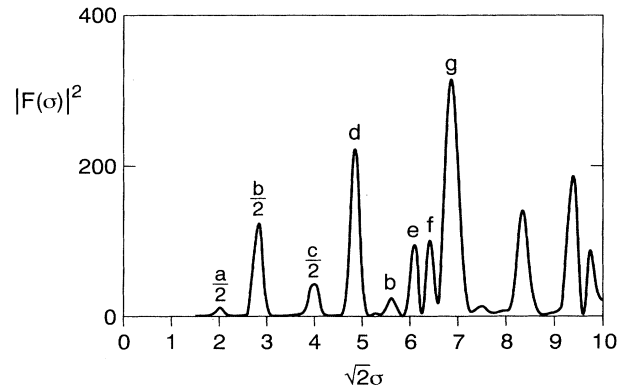


FIG. 17. Fourier spectrum versus scaled action σ .

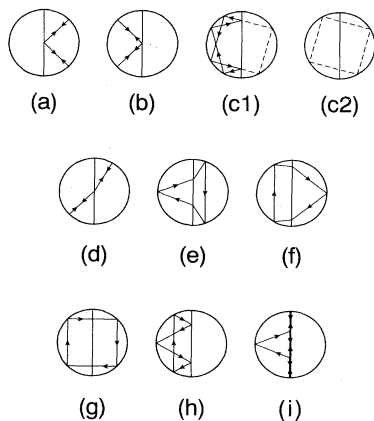


FIG. 18. Orbits corresponding to the first few spectral peaks. For the value $\eta=0.5$ used in Fig. 17 the peak at a (not labeled in Fig. 17) and the peak at $\frac{1}{2}c$ coincide. Another closed orbit not shown is that obtained by reflecting the closed orbit in (c1) through the y axis. For $\eta=\frac{1}{2}$ (as in Fig. 17) the action of this orbit is identical to that in (b) and so does not contribute a separate peak in addition to those labeled in Fig. 17.

axis. Thus the halves of orbits a , b , and c in the top half of the circle constitute periodic orbits of the up-down symmetric problem with one-half the action of orbits a , b , and c , and the corresponding peaks in Fig. 17 are labeled $\frac{1}{2}a$, $\frac{1}{2}b$, and $\frac{1}{2}c$. The orbits labeled h and i are discussed subsequently.

To provide further evidence that we have correctly identified the orbits with the peaks of $|F(\sigma)|^2$ we have varied η and verified that the numerically determined spectral peaks track our analytical calculations of the σ_j . This is shown in Fig. 19. The plotted dots give the locations of the various numerically determined spectral peaks for 50 values of η . The solid curves are trigonometrically determined analytical expressions for the reduced

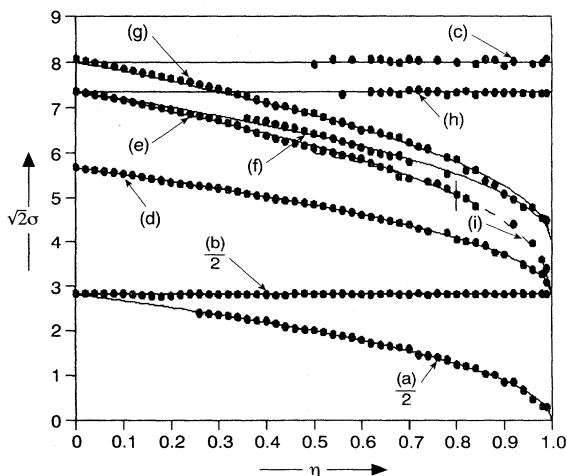


FIG. 19. Scaled actions of the orbits in Fig. 18 versus η . In this figure, for clarity, we include only those peaks (dots) that track the indicated labeled action curves.

actions. The orbits labeled (c) and (h) in Fig. 18 do not appear in the spectrum shown in Fig. 17 (which is done at $\eta=\frac{1}{2}$), but do appear at larger η (Fig. 19). (Presumably this is because the heights of their spectral peaks are proportional to the reflection coefficients raised to the fourth power, and this increases with increasing η .)

We now note a feature of Fig. 19 that appears to be a manifestation of the lateral ray [12] mentioned in Sec. I. The term “lateral ray” refers to the situation in which there appears a contribution to the Green’s function corresponding to the ray depicted in Fig. 20. In Fig. 20 the ray from the source travels to the boundary incident at the critical angle; it then travels laterally along the boundary on the high potential side, exits at the critical angle, and travels to the observation point. This contribution is in addition to the usual direct and reflected ray contributions, but is smaller than these by a factor of the order of the wavelength (see Ref. [12] and Appendix B). A trace formula including such lateral ray paths can be formulated. Thus the Fourier transform $F(\sigma)$ can exhibit peaks at closed “orbits” including lateral ray paths. An example of such a closed path is shown in Fig. 18(i). Note that the closed orbit of Fig. 18(e) only exists below a critical value of η . This critical value (at $\eta \approx 0.8$) is labeled in Fig. 19 by a short vertical line. The orbit in Fig. 18(i) exists for $1 \geq \eta \geq 0.5$. Its action closely (not exactly) follows the action of the orbit of Fig. 18(e), but extends past the critical η value where the orbit of Fig. 18(e) ceases to exist. The action of the lateral ray orbit in Fig. 18(i) is shown as a dashed line in Fig. 19 and appears to be an extension of the action of the Fig. 18(e) orbit past its critical η value. Thus the presence of observed peaks of $|F(\sigma)|^2$ (the dots in Fig. 19) that follow the dashed action curve ($\eta \gtrsim 0.8$) indicates a manifestation of the lateral ray in our spectra.

There are a number of interesting problems in the theory of the quasiclassical approximation that arise because of the existence of lateral rays (e.g., finding the lateral ray contribution amplitude in the Gutzwiller formula). We plan to address these problems in a future work.

VI. THE TRANSFER OPERATOR

The method of Bogomolny [13] provides a convenient way of doing the quasiclassical approximation. It is also known how to use this method to avoid the divergence problems encountered in the standard Gutzwiller approach. The method introduces an operator $T(q, q', E)$, which gives the semiclassical contribution for paths of energy E from a point q' on a surface of section to a final

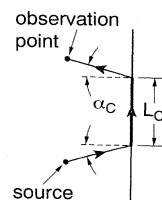


FIG. 20. (a) Lateral ray excited by a point source. (b) A closed ray orbit including a lateral ray path.

point labeled q crossing the surface of section for the first time. Paths passing n times through the surface of section are obtained by considering the n th power of the operator. Calculated in stationary phase, this yields the standard quasiclassical expressions.

The general form of a term of Bogomolny's operator is [13]

$$T(q, q', E) = \frac{1}{\sqrt{2\pi i \hbar}} \left[\left| \frac{\partial^2 S(q, q', E)}{\partial q \partial q'} \right| \right]^{1/2} \times e^{(i/\hbar)S(q, q', E) + i(\pi/2)\mu}. \quad (6.1)$$

Here a surface of section has been chosen and q measures distance along it. The action of a classical orbit of energy E from q' to its first return at q is denoted by $S(q, q', E)$ and μ is a Maslov index counting the points along the orbit where the simplest quasiclassical approximation breaks down. We shall measure the action in units of \hbar or, equivalently, choose units such that $\hbar = 1$.

In the present case, we take the surface of section as the boundary of the circle ∂C . We first write down the result for our problem, which, given Eq. (6.1), is quite intuitive. In Appendix A, we outline a formal derivation of the T operator. The left semicircle is described by $\pi/2 < \theta < 3\pi/2$ (denoted θ in C_L), while the right has $-\pi/2 < \theta < \pi/2$ (θ in C_R). Let $k_R = \sqrt{E - V_0}$ be the wave number for $x > 0$, while $k_L = \sqrt{E}$ is that for $x < 0$. If $E < V_0$ then $k_R = +i|k_R|$. We assume that $\sqrt{V_0} \gg 1$. The transfer operator is a sum of three terms

$$T = T_d + T_r + T_t, \quad (6.2)$$

whose orbits are illustrated in Fig. 21.

The direct orbit between θ and θ' that does not encounter the discontinuity at $x = 0$ gives a contribution

$$T_d(\theta, \theta') = - \left[\frac{k_{R,L}}{4\pi i} \left| \sin \frac{\theta - \theta'}{2} \right| \right]^{1/2} \times \exp \left[2ik_{R,L} \left| \sin \frac{\theta - \theta'}{2} \right| \right], \quad (6.3)$$

where we suppress the dependence on energy. The negative sign is a Maslov index counting one bounce from the circular boundary. The action is just the wave number times the chord length between the points on ∂C at θ, θ' .

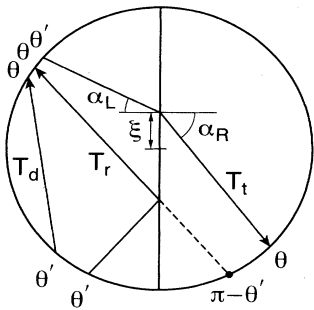


FIG. 21. Illustration of paths corresponding to T_d , T_r , and T_t in Eq. (6.2).

These two angles must both be either in C_R or C_L , respectively.

The contribution of the reflected orbit is

$$T_r(\theta, \theta') = -r_{R,L}(\theta, \theta') \left[\frac{k_{R,L}}{4\pi i} \left| \cos \frac{\theta + \theta'}{2} \right| \right]^{1/2} \times \exp \left[2ik_{R,L} \left| \cos \frac{\theta + \theta'}{2} \right| \right]. \quad (6.4)$$

Since such an orbit is generally split, we must extend the definition given in Eq. (6.1) and include the reflection coefficient $r_{R,L}(\theta, \theta')$ given by

$$r_L(\theta, \theta') = -r_R(\theta, \theta') = \frac{k_L \cos \alpha_L - k_R \cos \alpha_R}{k_L \cos \alpha_L + k_R \cos \alpha_R}, \quad (6.5)$$

where in this case $2\alpha_{L,R} = \theta - \theta'$ if $\theta, \theta' \in C_{L,R}$ and $\alpha_{L,R}$ are related by Snell's law Eq. (2.1). The physical meaning of α_L is that $k_L \cos \alpha_L$ is the component of the momentum perpendicular to the potential discontinuity, i.e., the x component of the momentum.

The contribution to the transfer operator for a transmitted orbit is

$$T_t(\theta, \theta') = \frac{-t(\theta, \theta')}{\sqrt{2\pi i}} \left[\left| \frac{\partial^2 S_t(\theta, \theta')}{\partial \theta \partial \theta'} \right| \right]^{1/2} e^{iS_t(\theta, \theta')}. \quad (6.6)$$

In Eq. (6.6) (where $\theta_<$ is the angle in C_L , $\theta_>$ is the angle in C_R , and θ, θ' are not on the same side)

$$S_t(\theta, \theta') = k_R L(\theta_>, \xi) + k_L L(\theta_<, \xi). \quad (6.7)$$

Here $L(\theta, \xi)$ is the distance from a point θ on the boundary to a point on the discontinuity at $x = 0$ a distance ξ from the center such that Snell's law is obeyed by the two rays. In fact, ξ is determined as that value which minimizes S_t of Eq. (6.7). [Given θ and θ' , $\xi(\theta, \theta')$ can be found as the solution of a quartic equation, but the result is so cumbersome that we have found it best to minimize Eq. (6.7) numerically.] The lengths are given by $L(\theta, \xi) = \sqrt{1 + \xi^2 - 2\xi \sin \theta}$. The transmission coefficient $t(\theta, \theta')$ in the prefactor is given by

$$t(\theta, \theta') = \frac{2\sqrt{k_L \cos \alpha_L k_R \cos \alpha_R}}{k_L \cos \alpha_L + k_R \cos \alpha_R}, \quad (6.8)$$

where $\tan \alpha_L = (\xi - \sin \theta_<)/\cos \theta_<$ and $k_R \cos \alpha_R = k_L \sqrt{\sin^2 \alpha_c - \sin^2 \alpha_L}$.

For angles $\alpha_L > \alpha_c$, the critical angle for internal reflection $k_R \cos \alpha_R$ becomes pure positive imaginary, the reflection coefficient has unit magnitude, and the transmitted wave is evanescent rather than propagating. In this case, the transmitted wave should be quasiclassically neglected [i.e., $T_t(\theta, \theta') = 0$].

It should be noted that t is the geometric mean of the transmission coefficients t_{RL}, t_{LR} of Eq. (2.5). An intuitive reason for this is that the fluxes through the surface are conserved, and the T operator is constructed to reflect that fact. This conservation is expressed by

$$|r(\theta', \theta)|^2 + |t(\theta'', \theta)|^2 = 1, \quad (6.9)$$

where the ray reflected from θ to θ' is split and transmitted to θ'' . In fact, the operator T is quasiclassically *unitary*, that is,

$$\int_{\partial C} d\theta T(\theta, \theta') \bar{T}(\theta, \theta'') \approx \delta(\theta' - \theta'') \quad (6.10)$$

when the integral is done in the stationary phase approximation. (Here \bar{T} denotes the complex conjugate of T .) Equation (6.10) requires Eq. (6.9) for its validity.

The T operator can be used to find contributions of very long trajectories, making many bounces from the boundary. We will here concentrate on eigenstates and eigenvalues. This information is obtained by solving

$$\int d\theta' T(\theta, \theta', E_a) \psi_a(\theta') = \psi_a(\theta). \quad (6.11)$$

Solutions will exist, of course, only for energies E_a causing $D(E) = \det[1 - T(E)]$ to vanish. In Appendix A we will see that, essentially, $\psi_a(\theta) \approx \partial\Psi(r, \theta)/\partial r|_{r=1}$, where Ψ solves Eq. (1.1).

A. The Gutzwiller trace formula

The Gutzwiller formula may be written [14], more generally than usual, as

$$\tilde{d}(E) = \frac{-1}{\pi} \text{Im} \frac{1}{D(E + i\eta)} \frac{dD(E)}{dE}, \quad (6.12)$$

where $D(E) = \det[1 - T(E)]$ is evaluated as the Fredholm determinant of the kernel T . The Fredholm expansions [14] of D and dD/dE are absolutely convergent. The series in E for \tilde{d} does not converge (for real E) because $D(E)$ vanishes on the spectrum. Clearly, at a zero E_a of D , there is a contribution $\delta(E - E_a)$ to $\tilde{d}(E)$. (In Ref. [14] it is shown that this formula also gives a contribution equal to the negative of the smoothed density of states.)

The Fourier technique of Sec. V does not rely on the convergence of the series for Eq. (6.12). Therefore, we do not worry about convergence and use the relation $\ln \det(1 - T) = \text{Tr} \ln(1 - T)$ to obtain

$$\tilde{d}(E) = \frac{1}{\pi} \text{Im} \sum_{s=1}^{\infty} \frac{1}{s} \frac{d}{dE} \text{Tr} T(E)^s = \frac{-1}{\pi} \text{Im} \sum_{s=1}^{\infty} \tilde{d}_s(E). \quad (6.13)$$

Equation (6.13) is more general than Eq. (5.1) in that it does not require that all orbits are hyperbolic unstable orbits. In particular, it works when there are stable orbits or nonisolated orbits present, as in the present model. The quantity \tilde{d}_s gives the contributions of all periodic orbits of "length" s , i.e., those making s bounces from ∂C .

Since the present model has both isolated periodic orbits and continuous families of periodic orbits, Eq. (6.13) must be used in place of Eq. (5.1) if amplitudes are to be correctly calculated. The actions are correctly given by both formulas.

A number of interesting points come up in calculating the amplitudes. These will be reported separately.

B. Numerical computation using the transfer operator

A simple and numerically rather straightforward method of using the transfer operator is to solve Eq.

(6.11) by discretization of the integral. There are a couple of points worth mentioning.

One could use other representations of the operator instead of the position on the surface of section. The maximum rate of change of T with respect to the variable θ' occurs in the exponent and is given by k_L . This indicates that the angular momentum representation $T_{mm'}$ will have large matrix elements only for $|m| < k_L$. In other words, $T_{mm'}$ will be approximately an $N \times N$ matrix, where $N = 2k_L = 4\pi/\lambda = 2 \times (\text{circumference})/(\text{wavelength})$. More precisely, the large elements of $T_{mm'}$ will be confined to an $N \times N$ submatrix. Combined with the approximate unitarity result, Eq. (6.10), this indicates that this $N \times N$ matrix is approximately unitary, so its eigenvalues will be close to the unit circle, while the eigenvalues coming from the small elements will be small.

A straightforward discretization of the angle will require several times more than N points, however, say R points. This gives an effective $R \times R$ matrix. Since there is a representation where the matrix is $N \times N$, one expects about N of the R eigenvalues of T to be close to the unit circle and the rest to be rather small.

The procedure is to choose an energy or wave number k_L , numerically obtain the eigenvalues of the $R \times R$ approximation to T , pick out one of them of the form $t_\gamma = ae^{i\omega(k_L)}$, where $a \approx 1$, and vary k_L until $\omega = 0$. The energy that makes the phase vanish gives an approximate quasiclassical solution of Eq. (6.11) and the corresponding eigenstate can be calculated.

This method, since it is an approximation to the boundary integral method, is efficient in the sense that the size of the matrix grows as \sqrt{E} , whereas the direct method [i.e., expanding Ψ in (1.1) as the product of sinusoids in angle and Bessel functions in radius] must diagonalize a matrix of size proportional to E . That substantial economy is partially offset by the necessity to find the zero of the eigenphase. (In addition, the complete wave functions are not so readily found and the programming effort is somewhat greater as well.)

We tested this method of direct diagonalization of T and compared the energy eigenvalues of even parity modes with the exact numerical answers. The results are compared with those obtained using the direct method in Table I. One sees that this approximate evaluation of the transfer operator eigenvalues is quantitatively effective.

One can also compute the eigenvectors corresponding to the eigenphases zero. In Fig. 22 we present the numerical plot of the absolute value of some even parity eigenvectors as a function of position on the boundary circle. They correspond essentially to the normal derivative of the wave function at the associated energy. These eigenvectors were arbitrarily chosen among the data. For comparison, in the insets to Fig. 22 we show the corresponding state as a function of position in the billiard determined using the direct method (as in Fig. 13).

VII. SCARS

Often there are eigenstates whose modulus squared shows the presence of scarring, i.e., enhanced magnitude along periodic ray orbits [10]. We discuss some scars

that appear in this model that have striking and unusual properties.

A. Internal reflection scars

Consider the states that seem to reflect from the center of the step at angles greater than critical (Fig. 14). We call these *internal reflection scars*. First note that such states *cannot* exist in a perfect semicircular billiard, with infinite potential on the diameter. Such a billiard is integrable and its states are a subset of the states of the circular billiard, namely, those odd under reflection through the diameter. These states are not localized in angle and consequently do not look like IRS's. In this system, any orbit passing through the center of the circle is part of a periodic orbit. There is a continuous infinity of such periodic orbits, all with the same action, and so these periodic orbits *are not isolated*. They are marginally unstable. As we shall show, localization in angle of wave density (and consequently IRS's) results from the angular dependence of the phase of the total internal reflection coefficient.

A simple theory of such scars features "second" WKB quantization. To do this, we note that for such orbits only the reflected orbit is important. Thus we approximate T by T_r of Eq. (6.4). Let the states desired be denoted $\psi(\theta)$. Such states, which classically pass close to the center, will have low angular momentum, but obviously will not have angular momentum zero, since that would make it independent of θ . It turns out that the state varies quite rapidly with θ , but much less rapidly than does T . In fact, we can parametrize $\psi(\theta)$ in WKB fashion as

$$\psi(\theta) = \sin[\sqrt{k_L} f(\theta)], \quad (7.1)$$

in $\pi/2 \leq \theta \leq 3\pi/2$, where the unknown function $f(\theta)$ is either even or odd about the x axis, $f(\theta) = \pm f(2\pi - \theta)$. (This respects the remaining symmetry of the problem.) The variation of f is on the scale of unity. One is led naturally to this particular choice of scale intermediate between k_L and unity as we shall soon see. We wish to solve

$$\int d\theta' T_r(\theta, \theta') \psi(\theta') = \psi(\theta). \quad (7.2)$$

Substituting the expression (7.1) for ψ , the integral in (7.2) is done in the spirit of stationary phase. We encounter the integrals $I_{\pm}(\theta)$

$$I_{\pm}(\theta) = - \int_{\pi/2}^{3\pi/2} d\theta' r(\theta, \theta') \left[\frac{k_L \cos[\frac{1}{2}(\theta + \theta')]}{4\pi i} \right]^{1/2} \times e^{2ik_L |\cos[(\theta + \theta')/2]|} e^{\pm i\sqrt{k_L} f(\theta')}. \quad (7.3)$$

The stationary point of the most rapid oscillations is at $\theta' = -\theta$. We thus expand the exponent in Eq. (7.3) about $-\theta$, i.e., $\cos[\frac{1}{2}(\theta + \theta')] \approx 1 - \frac{1}{8}(\theta + \theta')^2$; $f(\theta') \approx f(2\pi - \theta) + f'(2\pi - \theta)(\theta + \theta')$. This yields

$$I_{\pm} \approx i \exp[i\{2k_L + [f'(\theta)]^2 + \Phi(\theta)\}] e^{\pm i\sqrt{k_L} f(2\pi - \theta)}, \quad (7.4)$$

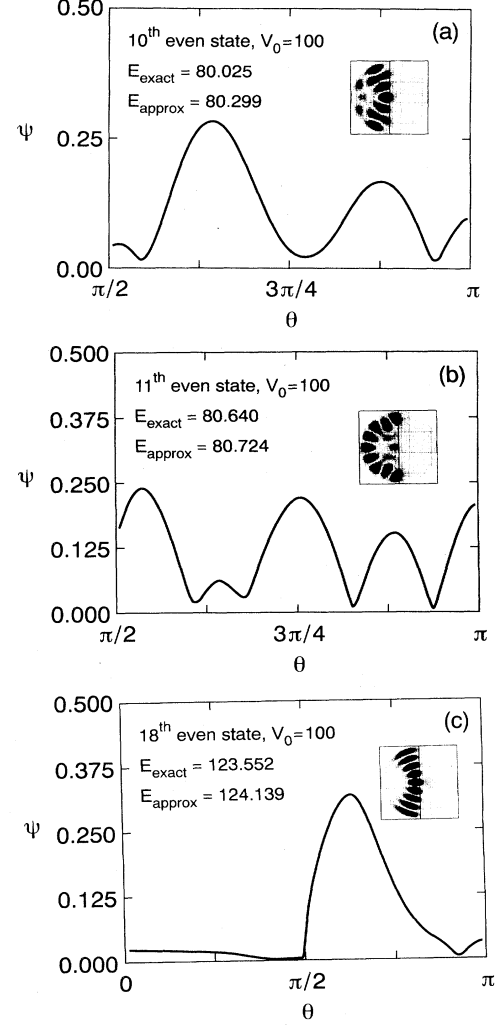


FIG. 22. Eigenfunctions of the transfer operator. Three examples of even eigenfunctions are given, together with the exact energy and the approximate energy determined by diagonalization of the transfer operator. The insets show the exact eigenfunctions in the representation used in Fig. 13. Note that states 10 and 11 are accidentally nearly degenerate and display a mixing between a pure IRS state and a whispering gallery state. This fairly delicate effect is reproduced quite well in the transfer operator approximation.

where the reflection coefficient $r(\theta, 2\pi - \theta) = e^{i\Phi(\theta)}$ is determined from Eq. (1.5) and Snell's law assuming $\eta > \cos^2 \alpha_L$, $\cos \alpha_R = |\cos \theta|$, and $k_R \cos \alpha_R = ik_L \sqrt{\eta - \cos^2 \theta}$. The phase of the reflection coefficient thus satisfies

$$\Phi(\theta) = -2 \arccos(|\cos \theta|/\eta). \quad (7.5)$$

In order to have a solution of Eq. (7.2) the first exponential in I_{\pm} must be equal to $\mp i$, in the even and odd cases, respectively. Therefore we have the condition

$$2k_L + [f'(\theta)]^2 + \Phi(\theta) = 2\pi(p \mp \frac{1}{4}), \quad (7.6)$$

where p is a positive integer. This condition is to deter-

TABLE I. Exact and semiclassical eigenvalues for $\eta = \frac{1}{3}$ and $\frac{1}{2}$ and for $V_0 = 100$.

No.	Exact E $\eta = \frac{1}{3}$	Semiclassical E $\eta = \frac{1}{3}$	Exact E $\eta = \frac{1}{2}$	Semiclassical E $\eta = \frac{1}{2}$	Exact E $V_0 = 100$	Semiclassical E $V_0 = 100$
1	3.407	3.552	3.674	3.834	6.538	6.568
2	9.091	9.188	10.566	10.741	18.550	18.598
3	15.418	15.923	16.523	17.185	21.932	21.990
4	17.774	18.040	19.359	19.505	35.048	35.099
5	25.169	25.424	28.241	28.735	43.058	43.138
6	30.369	30.543	34.239	34.374	46.296	46.434
7	34.308	34.196	39.098	39.661	55.827	55.890
8	40.564	41.519	42.687	43.244	68.768	68.904
9	44.024	44.113	49.983	50.298	75.297	75.432
10	47.076	46.996	51.869	51.713	80.025	80.299
11	57.953	58.685	63.196	64.077	80.640	80.724
12	60.068	60.223	69.221	69.166	98.094	98.410
13	63.455	63.680	70.213	70.840	105.777	106.115
14	72.152	73.006	76.198	77.377	108.334	108.899
15	74.676	74.807	82.384	82.688	110.538	110.351
16	76.919	77.385	87.696	88.145	114.351	115.029
17	82.783	82.920	95.422	95.630	120.042	120.276
18	90.044	89.934	99.968	100.451	123.552	124.137
19	93.011	93.185	103.755	103.810	125.932	126.085
20	102.521	103.426	110.298	110.715	131.122	131.520
21	107.419	107.050	119.221	119.273	136.838	137.573
22	107.898	108.247	120.846	121.293	142.445	142.720
23	112.625	113.074	121.677	122.538	144.704	144.935

mine k_L and thus the energy of the scar $E = k_L^2$.

Denoting

$$\varepsilon = 2\pi(p \mp \frac{1}{4}) - 2k_L, \quad (7.7)$$

we see that the condition (7.6) is a sort of WKB condition in which $(f')^2$ is a momentum squared or kinetic energy, Φ is a potential energy, and ε is the total energy. Note that Φ is an *attractive*, i.e., negative, potential. Comparing (7.7) with (4.1), we arrive at the expression $\gamma_p = \mp(1/4) - (\varepsilon/2\pi)$ for the defect γ_p . Equation (7.6) can be integrated to obtain $f(\theta)$,

$$f(\theta) = \int_{\pi/2}^{\theta} d\theta' \sqrt{\varepsilon - \Phi(\theta')} + \text{const.} \quad (7.8)$$

The next question is to determine ε and the constant of integration. We argue that $\psi(\theta) \sim \sin[\sqrt{k_L}f(\theta)]$ must vanish for $\theta \rightarrow \pi/2$. This follows from a side calculation in which both the direct and reflected orbits are included. For $\theta \rightarrow \pi/2$, these two orbits contribute with equal magnitude and opposite sign, since according to (7.5), $\Phi(\pi/2) = -\pi$. We satisfy this requirement by setting the constant of integration in (7.8) to $-l\pi/\sqrt{k_L}$, where l is a positive integer.

The value of ε is now determined by the second quantization condition. Two situations are possible. First, there may occur a turning point at an angle θ_c defined via $\Phi(\theta_c) = \varepsilon < 0$. At this point the positive and negative solutions for f' merge. This is illustrated in Fig. 23 by the higher curve and corresponds to the usual turning point case of WKB theory. Equation (7.2) can be expanded around this point with the result that $\psi(\theta)$ satisfies a second-order differential equation of the Airy type. Thus the appropriate value of $\sqrt{k_L}f(\theta_c)$ is $\pi/4$ accounting for

the phase change occurring at the turning point. This results in the quantization condition

$$\int_{\pi/2}^{\theta_c} d\theta \sqrt{\varepsilon - \Phi(\theta)} = \pi(l - 1/4) / \sqrt{k_L} \quad (7.9)$$

and $l = 1, 2, 3, \dots$

A numerical solution of (7.9) and (7.7) yields the smooth curve $\gamma_p = \frac{1}{4} - (\varepsilon/2\pi)$ versus p displayed in Fig. 15. Here the quantization index l is unity. As the index p and correspondingly k_L increase the critical angle θ_c , where $|\cos\theta_c| = \cos\alpha_c = \sqrt{V_0/k_L^2}$ moves toward $\pi/2$. This happens at a rate faster than k_L increases such that at some point, according to (7.9), it is no longer possible to find a solution with a turning point satisfying $\theta_c > \theta_e > \pi/2$. Physically, wave density diffracts out of the range of angles corresponding to total internal reflection and can then enter the high potential side of the circle. At this point the IRS's and CBS's probably merge, and a more refined theory is required to describe them.

The second situation occurs when $\eta = V_0/k_L^2 > 1$ and the particle is classically forbidden from the right-hand side. In this case there may or may not be a turning point in Eq. (7.9). The situation without a turning point is illustrated by the lower curve in Fig. 23. In this case, the quantization condition is determined by requiring that the wave function (7.1) be continuous at $\theta = \pm\pi$. For the case of odd modes we require $f(\pm\pi) = 0$ and for even modes $\sqrt{k_L}f(\pm\pi) = \pi/2$. The resulting quantization condition then is written

$$\int_{\pi/2}^{\pi} d\theta \sqrt{\varepsilon - \Phi(\theta)} = \pi(l + \delta) / \sqrt{k_L},$$

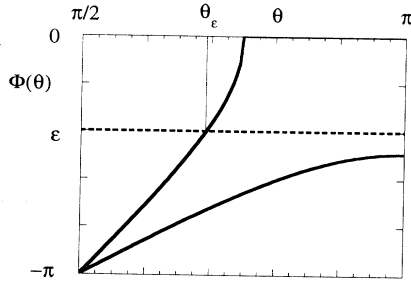


FIG. 23. Phase of the reflection coefficient versus angle for (a) $\eta = E/V_0 > 1$ showing a turning point at θ_E and (b) $\eta = E/V_0 < 1$ showing $\Phi(\theta) - \varepsilon > 0$ for all θ .

where $\delta = 0$ for odd modes and $\delta = \frac{1}{2}$ for even modes. In the above analysis, the index l is restricted by the requirement that the angular momentum be small $l \ll k_L$.

B. Central bounce scars

States such as the ones shown in Fig. 13 (18, 35, and 63), and probably those of Fig. 13 (17, 45, 47, 56, 62, and 69) (in addition to those in Fig. 14), are clearly strongly influenced by the classical orbits passing through the center of the circle. This suggests that an approximation along the lines of the preceding subsection might work, where, however, one must retain both T_r and T_t . We have not yet been able to find a formulation sufficiently simple to report here, and a fuller explanation of this type of scar must remain for the future.

C. Whispering gallery scars

The whispering gallery scars evident in Fig. 13 (1, 2, 4, 10, 14, 16, 26, 34, and 38–66) are well known in billiards. We present a simple theory for those WIGS's whose energy is less than V_0 .

For a circular billiard, angular momentum m is a good quantum number and the energy is determined by $J_m(k_{mn}) = 0$. The WIGS's for this case are states with the lowest value of energy for a given m .

For our model, angular momentum is not quantized. However, for large angular momentum we can still seek

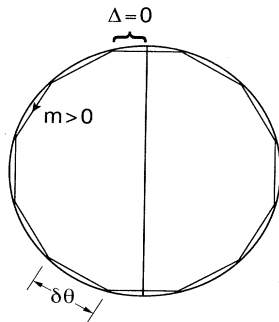


FIG. 24. WIGS orbit.

states concentrated near the circular boundary. Quasi-classically, except near the step, the state will not “know” that angular momentum is not conserved. We therefore take as an ansatz

$$\psi(\theta) = \begin{pmatrix} \cos \\ \sin \end{pmatrix} (m\theta), \quad (7.10)$$

where m is not an integer. We may imagine the state “penetrating” a bit into C_R , about to the first zero of ψ in that “classically forbidden” region. Beyond that, we take ψ to vanish.

In this case, we have no transmission possibility. Calculating

$$I_d(\theta) = \int_{\pi/2}^{3\pi/2} d\theta' T_d(\theta, \theta') e^{im\theta'} \quad (7.11)$$

in a stationary phase leads to

$$I_d(\theta) = \Delta(\theta) e^{i\beta(m, k_L)} e^{im\theta}, \quad (7.12)$$

where the phase is

$$\beta(m, k_L) = 2\sqrt{k_L^2 - m^2} - m\delta\theta - \frac{3\pi}{2}. \quad (7.13)$$

Here $\delta\theta = (m/|m|)2\cos^{-1}(m/k_L)$. A classical particle of angular momentum $m\hbar$ increments its angular position by this amount at each bounce.

For a circle, $\Delta = 1$, m is an integer, and the solution of $\beta(mk_{mn}) = 2\pi(n-1)$ is the semiclassical approximation to the n th zero k_{mn} of Bessel's m th function first found by Keller and Rubinow [16]. In our case, the stationary phase point $\theta' = \theta - \delta\theta$ is not in the domain of integration of (7.11) ($3\pi/2 > \theta' > \pi/2$) if $\pi/2 < \theta < \pi/2 + \delta\theta$ ($m > 0$) or $3\pi/2 - |\delta\theta| < \theta < 3\pi/2$, ($m < 0$), and we consequently take $\Delta(\theta) = 0$ in these ranges and unity otherwise. These conditions exclude those classical skips of size $\delta\theta$ arriving at θ from outside C_L . This geometry is illustrated in Fig. 24. Next, consider

$$I_r(\theta) = \int d\theta' T_r(\theta, \theta') e^{im\theta'} \quad (7.14)$$

as evaluated in stationary phase. It is not difficult to find that

$$I_r(\theta) = [1 - \Delta(\theta)] e^{i[\pi m + \Phi(k_L)]} e^{i\beta(m, k_L)} e^{-im\theta}. \quad (7.15)$$

According to this formula, the reflection reverses the angular momentum and, in addition to the standard phase β , it gives to the wave function an additional phase $\pi p = \pi m + \Phi(k_L)$. Therefore, we see that Eq. (7.10) is an eigenstate if, for the even cosine states p is an even integer and for the odd sine states p is odd.

The phase $\Phi(k_L)$ is the shift for normal incidence

$$\Phi(k_L) = -2\cos^{-1} \left[\frac{k_L}{\sqrt{V_0}} \right]. \quad (7.16)$$

At zero energy or infinite step height, $\Phi = -\pi$. In this case, m will be an even integer m_0 for odd states and an odd integer for the even states. This guarantees that the state vanishes at $\theta = \pm\pi/2$ as required.

The WIGS's of interest are those for $n = 1$ and

TABLE II. Energies and angular momenta of whispering gallery scars. The nominal angular momentum is in the first column, the "classical" angular momentum shifted by the reflection is in the second column, the energy in this approximation is in the third column, the exact energy is in the fourth column, and the energy for a semicircular billiard is in the last column.

m_0	$m(m_0, k)$	Semiclassical E	Exact E	E for semicircle
1	0.8	12.8	13	14.7
2	1.8	23.2	24	26.4
3	2.7	36.0	37.2	40.7
4	3.7	51.1	52.4	57.6
5	4.6	68.4	70	76.9
6	5.5	87.7	89.8	98.7
7	6.5	109.1	111.6	122.9
8	7.4	132.3	135.4	149.5
9	8.3	157.1	161.2	178.3
10	9.2	183	188.4	209.5

$p = m_0 - 1$. The actual "angular momentum" is $m(m_0, k) \equiv (m_0 - 1) - \Phi(k_L)/\pi$. Our approximate eigenenergies for the WIGS states are then given by the roots of

$$\beta(m(m_0, k_L), k_L) = 2\pi(n - 1), \quad (7.17)$$

which we have determined numerically for $n = 1, m_0 = 1, \dots, 10$, and $V_0 = 100$. In Table II we display exact energies of the corresponding states, those predicted by (7.17), and those for the semicircular billiard, corresponding to $\Phi = -\pi$. We also display the angular momentum m for the state. The agreement is quite reasonable. Note that even for the ground state $m_0 = 1$, the effect of reflection is not totally negligible, even when V_0 is fairly large.

It is also possible to find approximate energies for the "second-order" WIGS's, such as those in Fig. 13 (3, 5, and 8). These states have one radial node and are given by our approximate Eq. (7.17) with $n = 2$. The results are listed in Table III. These give energies that are too small. This may be because the classical orbits for such states do not impinge on the interface normally, as we assumed in the above derivation. Thus the effective phase for reflection Φ is closer to $-\pi$ than we have assumed, which would raise the energy.

TABLE III. Energies and angular momenta of second-order whispering gallery scars with one radial node. The entries are as in Table II.

m_0	$m(m_0, k)$	Semiclassical E	Exact E	E for semicircle
1	0.7	42.9	43.8	49.2
2	1.6	62.1	68	70.8
3	2.6	83.7	86.1	95.3
4	3.5	107.5	117.5	122.4
5	4.4	133.4	137.5	152.2
6	5.3	161	177.3	184.7
7	6.1	189.3	196.2	219.7

ACKNOWLEDGMENTS

The work of R.B. was supported by the Institute for Plasma Research at the University of Maryland. E.O. and T.M.A. were partially supported by the Office of Naval Research. R.E.P. and B.G. were partially supported by National Science Foundation Grant No. DMR-9114328. B.G. was partially supported by the French Ministry of Foreign Affairs.

APPENDIX A: EXACT FORMULATION OF THE TRANSFER FUNCTION

An alternative formulation to the problem of finding numerical solutions to Eq. (1.1) (and its boundary conditions) is given by the *boundary integral method* based on Green's theorem. Let $G(\mathbf{r}, \mathbf{r}', E)$ be the exact Green's function for this problem. Let $G_0(\mathbf{r}, \mathbf{r}', E)$ be the Green's function for *all space* that includes a jump in the potential at $x = 0$. In other words, G_0 satisfies Eq. (1.1), but not the boundary conditions on the circle. Green's identity gives

$$G(\mathbf{r}, \mathbf{r}', E) = G_0(\mathbf{r}, \mathbf{r}', E) - \int_{\partial C} d\theta G_0(\mathbf{r}, \mathbf{r}(\theta), E) \mu(\theta). \quad (A1)$$

We have used the fact that $G(\mathbf{r}, \mathbf{r}', E)$ vanishes on ∂C and have defined

$$\mu(\theta) = \partial G(\mathbf{r}(\theta), \mathbf{r}', E) / \partial n. \quad (A2)$$

Regarding \mathbf{r}' , E as parameters, we find an equation (a Fredholm equation of the second kind) for μ

$$\mu(\theta) = V_+(\theta) + \int_{\partial C} d\theta' K(\theta, \theta') \mu(\theta'), \quad (A3)$$

where $K(\theta, \theta') = -2\partial G_0(\mathbf{r}(\theta), \mathbf{r}(\theta'), E) / \partial n$ and $V_+(\theta) = 2\partial G_0(\mathbf{r}(\theta), \mathbf{r}', E) / \partial n$. [The factor 2 comes because $\partial G_0(\mathbf{r}, \mathbf{r}(\theta'), E) / \partial n$ has a δ -function singularity as $\mathbf{r} \rightarrow \mathbf{r}'$; this singularity is removed from K .] We remark that the *eigenenergies* and *eigenstates* are given by solutions of the *homogeneous* version of Eq. (A3)

The "bare" Green's function G_0 has a Fourier integral representation

$$G_0(\mathbf{r}, \mathbf{r}', E) = \frac{1}{2\pi} \int dk_y G_0(x, x', k_y, E) e^{ik_y(y-y')}, \quad (A4)$$

which consists of three pieces: a direct, a reflected, and a transmitted part. $G_0(x, x', k_y, E)$ is a one-dimensional Green's function, so it is easy to find that

$$G_0(x, x', k_y, E) = \begin{cases} \frac{1}{2ik_{Lx}} e^{ik_{Lx}|x-x'|} + \frac{r_L}{2ik_{Lx}} e^{ik_{Lx}|x+x'|} & \text{for } x, x' < 0 \\ \frac{1}{2ik_{Rx}} e^{ik_{Rx}|x-x'|} + \frac{r_R}{2ik_{Rx}} e^{ik_{Rx}|x+x'|} & \text{for } x, x' > 0 \\ \frac{1}{i(k_{Rx} + k_{Lx})} e^{ik_{Rx}x_{>} + ik_{Lx}|x_{<}|} & \text{for } xx' < 0. \end{cases} \quad (\text{A5})$$

Here $k_{L,Rx} = \sqrt{k_{L,R}^2 - k_y^2}$ and $x_{<,>}$ is the lesser, greater of x, x' . The reflection coefficients are $r_L = -(k_{Lx} - k_{Rx}) / (k_{Lx} + k_{Rx})$, $r_R = -r_L$. Except for the direct contributions, which are Hankel functions, the integral over k_y cannot be done in closed form. Note that although Eq. (2.4) has different transmission coefficients for RL and LR , this does not appear in the transmission component of G_0 . This is because the Green's function automatically takes into account flux conservation.

Perhaps the simplest method to evaluate (A4) is to make the substitution

$$k_y \rightarrow k_L \sin(\varphi), \quad k_{Lx} \rightarrow k_L \cos(\varphi),$$

which yields the integration path C_φ in the complex φ plane shown in Fig. 25. Since we are interested in the quasiclassical approximation, it is natural to do these integrals by the saddle point method. The leading saddle point approximation to G_0 yields the quasiclassical approximation to K , when the points $\mathbf{r} = (x, y)$ are placed on ∂C . (In the evaluation of K , consistent with the quasiclassical approximation, $-2\partial/\partial n$ is applied only to the exponential.) This approximation for K is in some sense close to $T(\theta, \theta')$. Actually, T is a symmetrized version of K , which is quite natural since K involves a one-sided normal derivative of G_0 . In fact, T is chosen so that it manifestly displays the flux conservation or unitarity property, which is not manifest in the operator K .

Consider the reflected ray in C_L . Call this contribution to the Green's function G_r . We find

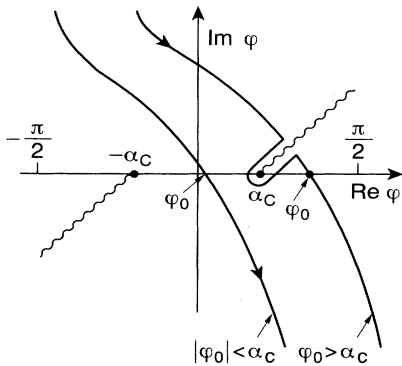


FIG. 25. Schematic steepest descent integration paths in the complex plane. In one case, a detour is needed to avoid a branch cut and this extra contribution gives the lateral ray.

$$G_r(x, x', y - y') = \frac{1}{4\pi i} \int_{C_\varphi} d\varphi r_L e^{ik_L \bar{r} \cos(\varphi - \varphi_0)}, \quad (\text{A6})$$

where $|x + x'| = \bar{r} \cos \varphi_0$ and $y - y' = \bar{r} \sin \varphi_0$. The phase is stationary at $\varphi = \varphi_0$, so a stationary phase evaluation yields

$$G_r(x, x', y - y') = \frac{r_L}{2i\sqrt{2\pi i}} \frac{e^{ik_L \bar{r}}}{\sqrt{k_L \bar{r}}}, \quad (\text{A7})$$

where r_L is evaluated at $\varphi = \varphi_0$. Now set $x = r \cos \theta$, $y = r \sin \theta$, $x' = r \cos \theta'$, and $y' = r \sin \theta'$. Follow this by taking the normal derivative, i.e., $\partial/\partial n = \partial/\partial r|_{r=1}$, again acting only on the exponent. Then

$$K_r(\theta, \theta') = \frac{-r_L}{\sqrt{2\pi i}} \left[\frac{k_L}{\bar{r}} \right]^{1/2} \frac{\partial \bar{r}}{\partial r} e^{ik_L \bar{r}}. \quad (\text{A8})$$

The expression for $T_r(\theta, \theta')$ is

$$T_r(\theta, \theta') = \frac{-r_L}{\sqrt{2\pi i}} \left[\frac{\partial^2(k_L \bar{r})}{\partial \theta \partial \theta'} \right]^{1/2} e^{ik_L \bar{r}}. \quad (\text{A9})$$

It is easy to find that $\partial \bar{r} / \partial r = \hat{n} \cdot \bar{\mathbf{r}} / \bar{r}$, where \hat{n} is the outward normal at θ . Similarly, the derivatives in the prefactor of T_r may be calculated. This yields the standard answer

$$T_r(\theta, \theta') = \left[\left| \frac{k'_n}{k_n} \right| \right]^{1/2} K_r(\theta, \theta'), \quad (\text{A10})$$

where k_n is the component of the momentum normal to ∂C of the ray arriving at θ and k'_n is the normal momentum of the initial ray.

We calculate T_i explicitly, since it is not completely obvious that the transmission coefficient of Eq. (6.8) is correct. Take, to be definite, $x_{>} = x$ and $x_{<} = x'$. Then

$$G_i(x, x', y - y') = \int \frac{dk_y}{2\pi i} \frac{e^{i[k_{Lx}|x'| + k_{Rx}x + k_y(y - y')]} }{k_{Lx} + k_{Rx}}. \quad (\text{A11})$$

The phase is stationary when k_y solves

$$y - y' - \frac{k_y}{k_{Lx}} |x'| - \frac{k_y}{k_{Rx}} x = 0. \quad (\text{A12})$$

Denote the derivative of this expression with respect to k_y by S_{kk} . Then

$$G_i = \frac{1}{\sqrt{2\pi i}} \frac{1}{k_{Lx} + k_{Rx}} \frac{e^{iS_i}}{\sqrt{|S_{kk}|}}. \quad (\text{A13})$$

Everything is evaluated at the stationary point and $S_t = k_{Lx}|x'| + k_{Rx}x + k_y(y - y')$. Setting $x = r \cos\theta$, etc. as before, taking the derivative of G_t with respect to r at $r = 1$ yields

$$K_t(\theta, \theta') = \frac{-2i}{\sqrt{2\pi i}} \frac{k_{Rx} \cos\theta + k_y \sin\theta}{k_{Lx} + k_{Rx}} \frac{e^{iS_t}}{\sqrt{S_{kk}}}. \quad (\text{A14})$$

Note that, since $\partial S_t / \partial k_y$ vanishes, one can ignore the dependence of k_y on r . This should be compared with

$$T_t(\theta, \theta') = \frac{-2}{\sqrt{2\pi i}} \frac{\sqrt{k_{Rx}k_{Lx}}}{k_{Lx} + k_{Rx}} \left[\frac{\partial^2 S_t}{\partial \theta \partial \theta'} \right]^{1/2} e^{iS_t}. \quad (\text{A15})$$

The cross derivative may be evaluated as

$$\frac{\partial^2 S_t}{\partial \theta \partial \theta'} = \frac{1}{S_{kk}} \left[\frac{k_y}{k_{Rx}} \sin\theta + \cos\theta \right] \left[\frac{k_y}{k_{Lx}} \sin\theta' + \cos\theta' \right]. \quad (\text{A16})$$

This in turn implies that

$$\begin{aligned} \frac{K_t}{T_t} &= \left[\frac{k_{Rx} \cos\theta + k_y \sin\theta}{k_{Lx} \cos\theta' + k_y \sin\theta'} \right]^{1/2} \\ &= \left[\frac{k_R \sin(\theta - \alpha_R)}{k_L \sin(\theta' - \alpha_L)} \right]^{1/2} = \left[\frac{k_{Rn}}{k_{Ln}} \right]^{1/2}. \end{aligned} \quad (\text{A17})$$

The angles are given in Fig. 21. Again, this is the canonical relationship involving the normal component of the momentum.

It should be noted that within the quasiclassical approximation these prefactors usually have little effect. This is because the magnitude of the normal component of the momentum is conserved at a bounce from ∂C . Therefore, if powers of T are evaluated in stationary

phase, prefactors systematically cancel. However, our notation hides the fact that the factors k_n depend on both θ and θ' , and furthermore, are different for direct, reflected, and transmitted rays. Therefore, the eigenfunctions of the T operator ψ are not precisely proportional to the eigenfunctions of the K operator, which are related to the solutions of (1.1) by $\mu(\theta) = \partial \Psi(r, \theta) / \partial r|_{r=1}$. However, $\psi(\theta) \approx \mu(\theta)$ up to a slowly varying factor.

APPENDIX B: LATERAL RAYS

In doing the integral for the reflected rays, it is to be noted that the prefactor [Eq. (A5)] is not analytic. The saddle point is at $\varphi = \varphi_0$, where $\tan \varphi_0 = (y - y') / |x + x'|$. The function $k_{Rx}(\varphi) = k_L \sqrt{\sin^2 \alpha_c - \sin^2 \varphi}$ has a branch cut at $\varphi = \alpha_c$, the critical angle for total internal reflection. For $|\varphi_0| < \alpha_c$, the contour can be chosen to pass over the saddle point, staying clear of the branch point. On the other hand, for $|\varphi_0| > \alpha_c$, the steepest descent contour is required to pass around the branch point, which gives an additional, somewhat smaller, contribution. This contribution has an action $S_{\text{lat}} = k_0 |x + x'| / \cos \alpha_c + k_0 L_c \sin \alpha_c$, where $L_c = |y - y'| - |x + x'| \tan \alpha_c$. This action can be interpreted as belonging to the path in Fig. 20, which slides along the interface laterally for a distance L_c . Evaluation of the integral gives

$$G_{\text{lat}} = e^{iS_{\text{lat}}} \frac{e^{3\pi i/4}}{\sqrt{\pi/2}} \frac{k_L^2}{V_0} \frac{[\tan \alpha_c]^{1/2}}{[k_L L_c]^{3/2}}. \quad (\text{B1})$$

This contribution is smaller than the main term by a factor of order $[k_L L_c]^{-1}$. When $|\varphi_0|$ is close to α_c , so that $[k_L L_c]^{-1}$ is not small, the simplest expression is not adequate. We do not record the contribution to the lateral wave Green's function in this case.

-
- [1] M. C. Gutzwiller, *Chaos in Classical and Quantum Mechanics* (Springer-Verlag, Berlin, 1990).
- [2] F. Haake, *Quantum Signatures of Chaos* (Springer-Verlag, Berlin, 1991).
- [3] E. Ott, *Chaos in Dynamical Systems* (Cambridge University Press, Cambridge 1993), Chap. 10.
- [4] A. M. Ozorio de Almeida, *Hamiltonian Systems: Chaos and Quantization* (Cambridge University Press, Cambridge, 1988).
- [5] L. Couchman, E. Ott, and T. M. Antonsen, Jr., *Phys. Rev. A* **46**, 6193 (1992).
- [6] R. N. Oerter, E. Ott, T. M. Antonsen, Jr., and P. So (unpublished).
- [7] R. L. Weaver, *J. Acoust. Soc. Am.* **85**, 1001 (1989).
- [8] D. Delande, D. Sornette, and R. Weaver, *J. Acoust. Soc. Am.* **93**, 1873 (1994).
- [9] C. Ellegaard, T. Guhr, K. Lindemann, H. Q. Lorensen, J. Nygard, and M. Oxborrow, *Phys. Rev. Lett.* **75**, 1546 (1995).
- [10] E. J. Heller, *Phys. Rev. Lett.* **53**, 1515 (1984).
- [11] For example, see U. Eichmann, K. Richter, D. Wintgen, and W. Sandner, *Phys. Rev. Lett.* **61**, 2438 (1988). In the elastic wave experiment of Ref. [8], Fourier transforms of the spectral fluctuations were also taken, yielding a few rather broad peaks. These peaks were attributed to "bouncing ball" orbits normally incident on the boundaries. Thus they did not involve ray splitting, since P and S waves [see Fig. 1(b)] do not couple at normal incidence.
- [12] L. M. Brekhovskikh, *Waves in Layered Media* (Academic, New York, 1960).
- [13] E. B. Bogomolny, *Nonlinearity* **5**, 805 (1992).
- [14] B. Georgeot and R. E. Prange, *Phys. Rev. Lett.* **74**, 2851 (1995).
- [15] We discuss the contribution to $\Delta \bar{N}(E)$ from a ray splitting boundary elsewhere [R. E. Prange, E. Ott, T. M. Antonsen, B. Georgeot, and R. Blümel, *Phys. Rev. E* **53**, 207 (1996)].
- [16] J. B. Keller and S. I. Rubinow, *Ann. Phys. (N.Y.)* **9**, 24 (1960).